

# A novel two loop inverse seesaw model

Gonzalo Benítez-Irarrázabal\*

*Departamento de Física, Universidad Técnica Federico Santa María, Casilla 110-V, Valparaíso, Chile*

Rocío Branada Balbontín†

*Instituto de Física, Pontificia Universidad Católica de Valparaíso, Casilla 4950, Valparaíso 2373223, Chile and  
Departamento de Física, Universidad Técnica Federico Santa María, Casilla 110-V, Valparaíso, Chile*

Cesar Bonilla‡

*Departamento de Física, Universidad Católica del Norte,  
Avenida Angamos 0610, Casilla 1280, Antofagasta, Chile*

A. E. Cárcamo Hernández§

*Universidad Técnica Federico Santa María, Casilla 110-V, Valparaíso, Chile  
Centro Científico-Tecnológico de Valparaíso, Casilla 110-V, Valparaíso, Chile and  
Millennium Institute for Subatomic Physics at High-Energy Frontier (SAPHIR), Fernández Concha 700, Santiago, Chile*

Sergey Kovalenko¶

*Departamento de Física y Astronomía, Universidad Andrés Bello, Sazié 2212, Piso 7, Santiago, Chile  
Millennium Institute for Subatomic Physics at High-Energy Frontier (SAPHIR), Fernández Concha 700, Santiago, Chile and  
Centro Científico-Tecnológico de Valparaíso, Casilla 110-V, Valparaíso, Chile*

Juan Marchant González\*\*

*Laboratorio de Cómputo de Física (LCF-UPLA),  
Facultad de Ciencias Naturales y Exactas, Universidad de Playa Ancha,  
Subida Leopoldo Carvallo 270, Valparaíso, Chile.*

We propose a Standard Model (SM) extension where neutrinos get masses through a two-loop inverse seesaw mechanism. This naturally explains the smallness of the neutrino masses and allows seesaw mediators to be at the TeV scale with testable phenomenology. The model adds two real singlet scalars and four electrically neutral leptons to the SM. The extension considers the existence of two global Abelian symmetries, a continuous  $U(1)$  and a discrete  $Z_3$ . The latter, remains unbroken after spontaneous symmetry breaking and forbids tree-level and one-loop neutrino masses, and stabilizes the dark matter (DM) candidates. This setup accommodates neutrino-oscillation data, yields two pseudo-Dirac heavy pairs with small active–sterile mixing, and predicts an effective Majorana mass  $m_{ee}$  in the 2.1–4.4 meV range for normal ordering. Charged-lepton flavor violation is naturally suppressed yet testable: for a representative benchmark we obtain  $\text{BR}(\mu \rightarrow e\gamma) \simeq 1.6 \times 10^{-14}$ , with correlated signals in  $\mu \rightarrow eee$  and  $\mu \rightarrow e$  conversion within next-generation experimental reach. Altogether, the radiative origin of neutrino masses links low-energy flavor observables to collider signatures, delineating discovery targets for MEG II, Mu2e/COMET, and the HL-LHC and distinguishing this framework from conventional inverse- and radiative-seesaw models. Moreover, the  $Z_3$  guarantees a stable DM candidate, either scalar ( $\rho$ ) or fermionic ( $\Omega$ ). Then, here we analyze and identify the viable parameter space that is consistent with the observed DM relic abundance for both situations.

---

\*Electronic address: [gonzalo.benitezi@usm.cl](mailto:gonzalo.benitezi@usm.cl)

†Electronic address: [rocio.branada@sansano.usm.cl](mailto:rocio.branada@sansano.usm.cl)

‡Electronic address: [cesar.bonilla@ucn.cl](mailto:cesar.bonilla@ucn.cl)

## I. INTRODUCTION

The presence of dark matter (DM) and the tiny masses of active neutrinos stand out as strong motivations for physics beyond the Standard Model (BSM). A minimal BSM extension that introduces right-handed (RH) Majorana neutrinos can generate neutrino masses via the type-I seesaw mechanism [1–7]. However, achieving the correct neutrino mass scale in this framework typically requires either extremely large (RH) Majorana masses or highly suppressed Dirac Yukawa couplings. Consequently, the mixing between light and heavy neutrinos becomes negligible, leading to extremely suppressed rates for charged lepton flavor violating (CLFV) processes—well below the reach of current experimental detection. In addition, such a minimal seesaw model does not provide a stable dark matter (DM) candidate to explain the observed DM relic density.

A natural connection between the neutrino mass generation and a stable dark sector comes out in theories of radiative neutrino masses, see for instance Ref. [8] for a review and Refs. [9, 10] for comprehensive studies of one- and two-loop radiative neutrino mass models. The minimal scenario introduces  $Z_2$ -odd particles to the SM, RH-neutrinos and a  $SU(2)$  scalar doublet which does not develop a vacuum expectation value (vev) as described in Ref. [11] for the first time. The  $Z_2$  symmetry remains intact after spontaneous symmetry breaking, stabilizes the DM candidates, and prevents neutrino masses at tree-level.

An attractive alternative is offered by models that realize the inverse seesaw mechanism [12–46]. These scenarios attribute the smallness of active neutrino masses to a tiny Majorana mass term that softly breaks lepton number symmetry. This term can itself be generated radiatively at one or more loop levels. Notably, the inverse seesaw allows for sizable mixings between active and heavy neutrinos, enabling CLFV rates that may be accessible in forthcoming experiments. When embedded in radiative or “scotogenic” setups, inverse seesaw models can simultaneously address dark matter and neutrino mass generation. In such models, some of the neutral seesaw mediators can serve as viable dark matter candidates, stabilized by the same discrete symmetries that forbid tree-level neutrino masses. The correct relic abundance can be achieved through dark matter annihilations into Standard Model or additional BSM particles within suitable regions of parameter space.

The inverse seesaw mechanism offers a viable framework for resonant leptogenesis, facilitated by the small mass splitting of heavy pseudo-Dirac neutral leptons [35–37, 41, 44, 47–52]. In this paper, we present an SM extension where active neutrino masses arise radiatively via a two-loop inverse seesaw. The model extends the SM particle content with just two gauge-singlet scalars and a minimal set of neutral leptons, while incorporating an additional global  $U(1)_X$  symmetry and a discrete  $Z_3$  symmetry. In our proposed model, the spontaneous breaking of the  $U(1)_X$  symmetry occurs, whereas the  $Z_3$  symmetry remains intact, enabling the radiative generation of a lepton-number-violating Majorana mass terms at two loops with the same topology of the Zee-Babu mechanism. The preserved  $Z_3$  symmetry in our model also ensures stable dark matter candidates, both scalar and fermionic. The proposed framework aligns with neutrino oscillation data and satisfies constraints arising from charged lepton flavor violation, dark matter relic abundance, and direct/indirect detection dark matter experiments. Our proposed model, has the following advantages with respect with the Zee-Babu model: 1) It incorporates Dark Matter candidates in the neutrino mass generation mechanism, which corresponds to a scotogenic feature, absent in the Zee Babu model. 2) Our model has two pairs of nearly degenerate Pseudo-Dirac leptons, whose small mass splitting, corresponding to the two loop level induced lepton number violating mass parameter is crucial for achieving successful TeV scale leptogenesis. The paper is organized as follows. We discuss the proposed model in Sec. II. The scalar potential is discussed in Sec. III. In Sec. IV, we discuss the neutrino sector and how the masses arise. In Sec. V, we presented a framework in which a singlet scalar and a fermionic DM candidate are studied separately and are contrasted with experimental

---

§Electronic address: [antonio.carcamo@usm.cl](mailto:antonio.carcamo@usm.cl)

¶Electronic address: [sergey.kovalenko@unab.cl](mailto:sergey.kovalenko@unab.cl)

\*\*Electronic address: [juan.marchant@upla.cl](mailto:juan.marchant@upla.cl)

	$l_{iL}$	$l_{iR}$	$\nu_{kR}$	$N_{kR}$	$\Omega_{kL}$	$\Omega_{kR}$	$\phi$	$\rho$	$\sigma$
$SU(3)_C$	1	1	1	1	1	1	1	1	1
$SU(2)_L$	2	1	1	1	1	1	2	1	1
$U(1)_Y$	$-\frac{1}{2}$	-1	0	0	0	0	$\frac{1}{2}$	0	0
$U(1)_X$	1	1	1	-1	-1	0	0	0	-1
$\mathbb{Z}_3$	0	0	0	0	-1	-1	0	-1	0

Table I: Charge assignments of leptonic and scalar fields of the model under the group  $SU(3)_C \times SU(2)_L \times U(1)_Y \times U(1)_X \times \mathbb{Z}_3$ . Here  $i = 1, 2, 3$  and  $k = 1, 2$ .

measurements and projections. In Sec. VI, we discuss some sizeable CLFV rates. Our conclusions are stated in section VII. In Appendix A we provide a discussion of the two-loop integral for the inverse seesaw  $\mu$ -entry in our model.

## II. THE MODEL

We propose the Standard Model (SM) extension with a spontaneously broken global  $U(1)_X$  and an exact  $\mathbb{Z}_3$  discrete symmetries. The field content is enlarged with two electrically neutral, real gauge singlet scalars  $\rho$  and  $\sigma$ , and with two generations ( $n = 1, 2$ ) of neutral leptons  $\nu_{nR}$ ,  $N_{nR}$ ,  $\Omega_{nL}$ , and  $\Omega_{nR}$ . In this setup, the tiny masses of the active neutrinos arise from an *inverse seesaw mechanism* realized at the two-loop level. The preserved  $\mathbb{Z}_3$  symmetry plays a dual role: it (i) forbids any tree-level mixing between  $N$  and  $\Omega$ , thereby eliminating a tree-level (and one-loop) source for the lepton-number-violating (LNV) submatrix  $\mu$  in the inverse-seesaw mass matrix, fixing the dominant two-loop topology for  $\mu$  and (ii) stabilizes the Dark Matter candidates of the model.

The model matter content and its charge assignments under the new symmetries is summarized in Table II. The Standard Model quarks are assumed to transform trivially under the new symmetries. Notice that  $\mathbb{Z}_3$  is the smallest Abelian group that promotes the two-loop origin of  $\mu$ .

The scalar fields are written as follows,

$$\phi = \begin{pmatrix} \phi^+ \\ \frac{v_\phi + h + i\xi}{\sqrt{2}} \end{pmatrix}, \quad \sigma = \frac{v_\sigma + \sigma_R + i\sigma_I}{\sqrt{2}}, \quad \rho = \frac{\rho_R + i\rho_I}{\sqrt{2}}, \quad (1)$$

where  $\phi$  is the SM Higgs doublet, and  $\sigma, \rho$  are singlets. Here,  $v_\phi \approx 246$  GeV. Then, only the SM gauge doublet  $\phi$  and the gauge singlet scalar  $\sigma$  participate in the spontaneous symmetry breaking after getting vacuum expectation values (VEVs) given by,

$$, \quad \langle \phi \rangle = \begin{pmatrix} 0 \\ \frac{v_\phi}{\sqrt{2}} \end{pmatrix}, \quad \langle \sigma \rangle = \frac{v_\sigma}{\sqrt{2}} \quad (2)$$

we get the following sequential symmetry breaking pattern:

$$\begin{aligned} \mathcal{G} &\equiv SU(3)_C \times SU(2)_L \times U(1)_Y \times U(1)_X \times \mathbb{Z}_3 \xrightarrow{v_\sigma} \\ &SU(3)_C \times SU(2)_L \times U(1)_Y \times \mathbb{Z}_3 \xrightarrow{v_\phi} \\ &SU(3)_C \times U(1)_Q \times \mathbb{Z}_3 \end{aligned} \quad (3)$$

where the global  $U(1)_X$  symmetry is spontaneously broken by the scalar singlet VEV  $v_\sigma$ , then the SM model gauge symmetry gets broken by the scalar doublet VEV  $v_\phi$ . The Abelian  $\mathbb{Z}_3$  symmetry is preserved after spontaneous symmetry breaking just like color and electric charge.

### III. SCALAR POTENTIAL

The most general scalar potential invariant under the symmetry described in the Table I, reads as:

$$V = -\mu_\phi^2(\phi^\dagger\phi) - \mu_\sigma^2(\sigma^\dagger\sigma) + \mu_\rho^2(\rho^\dagger\rho) + A[\rho^3 + h.c.] + \lambda_\phi(\phi^\dagger\phi)^2 + \lambda_\sigma(\sigma^\dagger\sigma)^2 + \lambda_\rho(\rho^\dagger\rho)^2 + \lambda_{\phi\sigma}(\phi^\dagger\phi)(\sigma^\dagger\sigma) + \lambda_{\phi\rho}(\phi^\dagger\phi)(\rho^\dagger\rho) + \lambda_{\sigma\rho}(\sigma^\dagger\sigma)(\rho^\dagger\rho). \quad (4)$$

Due to the global  $U(1)_X$  and the discrete  $Z_3$  symmetries, there is only one trilinear interaction in the scalar potential, i.e.,  $A(\rho^3 + h.c.)$ . As a result and due to the fact that  $\langle\rho\rangle = 0$ , there is no splitting between  $m_{\rho_R}$  and  $m_{\rho_I}$  neither Higgs- $\rho$  mixing in our model. The former means that  $\rho$  is a complex SM-singlet scalar  $\rho$  with the mass

$$m_\rho^2 = \mu_\rho^2 + \frac{1}{2}\lambda_{\rho\sigma}v_\sigma^2 + \frac{1}{2}\lambda_{\phi\rho}v_\phi^2. \quad (5)$$

The absence of the Higgs- $\rho$  mixing, as will be explained in Section VB1, results in loop suppression of the scattering of our fermionic DM candidate  $\Omega$  on nuclei. This allows relaxation of the limits from direct DM detection on the relic density.

The imaginary (CP-odd) part  $\sigma_I$  of the SM-singlet scalar  $\sigma$ , as defined in (1), is the massless Nambu-Goldstone boson resulting from the spontaneous breaking of the global  $U(1)_X$  symmetry.

From the minimization conditions for the scalar potential (4) we find

$$\mu_\phi^2 = \lambda_\phi v_\phi^2 + \frac{1}{2}\lambda_{\phi\sigma}v_\sigma^2 \quad \mu_\sigma^2 = \lambda_\sigma v_\sigma^2 + \frac{1}{2}\lambda_{\phi\sigma}v_\phi^2.$$

Taking into account these relationships we obtain the squared mass matrix for the CP-even states

$$M_{\phi\sigma}^2 = \begin{pmatrix} 2\lambda_\phi v_\phi^2 & \lambda_{\phi\sigma}v_\sigma v_\phi \\ \lambda_{\phi\sigma}v_\sigma v_\phi & 2\lambda_\sigma v_\sigma^2 \end{pmatrix}, \quad (6)$$

in the basis  $(h, \sigma_R)$ . Now, the physical fields can be found using a matrix rotation

$$\begin{pmatrix} \tilde{\sigma} \\ \tilde{\Phi} \end{pmatrix} = \begin{pmatrix} \cos\theta_{\phi\sigma} & -\sin\theta_{\phi\sigma} \\ \sin\theta_{\phi\sigma} & \cos\theta_{\phi\sigma} \end{pmatrix} \begin{pmatrix} \sigma_R \\ h \end{pmatrix},$$

where  $\theta_{\phi\sigma}$  is the angle of rotation, which depends on some of the scalar potential parameters

$$\tan 2\theta_{\phi\sigma} = \frac{\lambda_{\phi\sigma}v_\sigma v_\phi}{\lambda_\sigma v_\sigma^2 - \lambda_\phi v_\phi^2}. \quad (7)$$

#### A. Stability conditions

In order to determine the stability conditions of the scalar potential, one has to analyze its quartic terms because they will dominate the behavior of the scalar potential in the region of very large values of the fields components. Then, to study these conditions we introduce the following Hermitian bilinear combination of the scalar fields

$$a = \phi^\dagger\phi, \quad b = \sigma^*\sigma, \quad c = \rho^*\rho.$$

Substituting these bilinears in the scalar potential (4), the quartic terms get the form,

$$V_4 = \lambda_\phi a^2 + \lambda_\sigma b^2 + \lambda_\rho c^2 + \lambda_{\phi\sigma}ab + \lambda_{\phi\rho}ac + \lambda_{\sigma\rho}bc, \quad (8)$$

which can be recast as

$$\begin{aligned}
V_4 = & \left( \sqrt{\lambda_\sigma} b - \sqrt{\lambda_\rho} c \right)^2 + \left( \sqrt{\lambda_\sigma} b - \sqrt{\lambda_\phi} a \right)^2 \\
& + \left( \sqrt{\lambda_\rho} c - \sqrt{\lambda_\phi} a \right)^2 + \left( \lambda_{\phi\rho} + 2\sqrt{\lambda_\rho\lambda_\phi} \right) ac \\
& + \left( \lambda_{\sigma\rho} + 2\sqrt{\lambda_\sigma\lambda_\rho} \right) bc + \left( \lambda_{\phi\sigma} + 2\sqrt{\lambda_\sigma\lambda_\phi} \right) ab \\
& - 2 \left( \lambda_\phi a^2 + \lambda_\sigma b^2 + \lambda_\rho c^2 \right)
\end{aligned} \tag{9}$$

Following the criteria described in Refs. [53, 54], we find that the stability conditions for this model are

$$\begin{aligned}
\lambda_\phi \geq 0, \quad \lambda_\sigma \geq 0, \quad \lambda_\rho \geq 0, \\
\lambda_{\phi\sigma} + 2\sqrt{\lambda_\phi\lambda_\sigma} \geq 0, \quad \lambda_{\phi\rho} + 2\sqrt{\lambda_\phi\lambda_\rho} \geq 0, \quad \lambda_{\sigma\rho} + 2\sqrt{\lambda_\sigma\lambda_\rho} \geq 0.
\end{aligned} \tag{10}$$

#### IV. NEUTRINO MASSES

With the particle content and symmetries specified in Table I, the Yukawa Lagrangian for the neutrino sector is given by

$$\begin{aligned}
-\mathcal{L}_Y^{(\nu)} = & \sum_{i=1}^3 \sum_{k=1}^2 (y_\nu)_{ik} \bar{\ell}_{iL} \tilde{\phi} \nu_{kR} + \sum_{n,k=1}^2 M_{nk} \bar{\nu}_{nR} N_{kR}^C + \sum_{n,k=1}^2 (y_N)_{nk} \bar{\Omega}_{kL} \rho N_{nR} \\
& + \sum_{n,k=1}^2 (z_\Omega)_{nk} \bar{\Omega}_{nR}^C \rho \Omega_{kR} + \sum_{n,k=1}^2 (y_\Omega)_{nk} \bar{\Omega}_{nL} \sigma \Omega_{kR} + \text{h.c.}
\end{aligned} \tag{11}$$

After spontaneous breaking (3) the neutrino mass matrix turns out to be

$$M_\nu = \begin{pmatrix} 0_{3 \times 3} & m_D & 0_{3 \times 2} \\ m_D^T & 0_{2 \times 2} & M \\ 0_{2 \times 3} & M^T & \mu \end{pmatrix}, \tag{12}$$

where  $m_D$  is a Dirac mass matrix, while  $M$  and  $\mu$  are Majorana matrices parametrized as

$$m_D = \frac{v_\phi}{\sqrt{2}} \begin{pmatrix} y_{\nu_{11}} & y_{\nu_{12}} \\ y_{\nu_{21}} & y_{\nu_{22}} \\ y_{\nu_{31}} & y_{\nu_{32}} \end{pmatrix}, \quad M = \begin{pmatrix} M_{11} & M_{12} \\ M_{12} & M_{22} \end{pmatrix} = \begin{pmatrix} M_1 & 0 \\ 0 & M_2 \end{pmatrix}, \quad \mu = \begin{pmatrix} \mu_{11} & \mu_{12} \\ \mu_{12} & \mu_{22} \end{pmatrix}, \tag{13}$$

where we have assumed the matrix  $M$  as diagonal.

The two-loop contribution to the Majorana mass submatrix  $\mu$ , shown in Figure 1, can be expressed in terms of the model parameters as

$$\mu = 3A y_N M_\Omega z_\Omega^* M_\Omega^T y_N^T I(m_\Omega, m_\rho), \tag{14}$$

where the two-loop integral  $I(m_\Omega, m_\rho)$  is defined and evaluated in Appendix A. Using (A8), we get

$$\mu \approx \frac{6}{(16\pi^2)^2} A y_N z_\Omega^* y_N^T \frac{m_\rho^4}{m_\Omega^4} z, \tag{15}$$

where the constant  $z \approx 1.56$  is derived in Appendix A. For simplicity, we assumed that a  $2 \times 2$  mass matrix  $M_\Omega$  of  $\Omega$  field is approximately diagonal with equal entries  $m_\Omega = y_\Omega v_\sigma$ . From this formula, the parameter  $\mu$  is small due to the two loop suppression of order  $(16\pi^2)^{-2} \sim 10^{-5}$  without requiring small Yukawa couplings  $y_N, z_\Omega$ . Sizable Yukawa couplings have important consequences in the DM phenomenology. This is discussed below in Section VB.

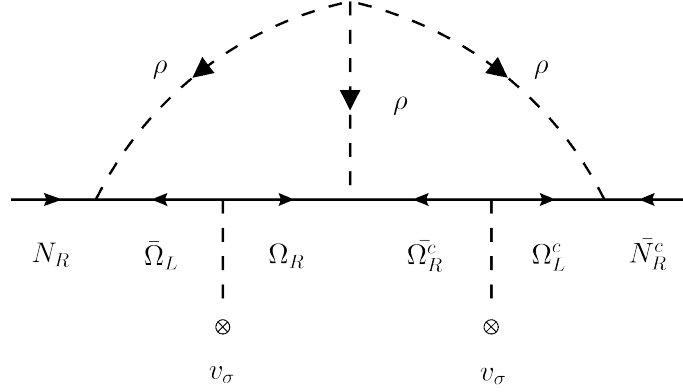


Figure 1: Two-loop Feynman diagram contributing to the Majorana neutrino mass submatrix  $\mu$ .

Note that the trilinear term  $A\phi^3$  in the scalar potential (4) softly breaks an accidental global  $U'(1)$  symmetry with charge assignments  $Q'(\rho) = 2, Q'(\Omega_R) = -1, Q'(\Omega_L) = 2, Q'(\sigma) = 3$ . Consequently, a small value for parameter A is technically natural and can therefore be consistently chosen.

The neutrino mass matrix from Eq. (12) can be diagonalized with the rotation matrix [41, 55]:

$$\mathbb{U} \simeq \begin{pmatrix} \left(1_{3 \times 3} - \frac{R_1 R_1^\dagger}{2}\right) \left(1_{3 \times 3} - \frac{R_2 R_2^\dagger}{2}\right) R_\nu & R_1 R_M^{(1)} & R_2 R_M^{(2)} \\ -\frac{R_1^\dagger + R_2^\dagger}{\sqrt{2}} R_\nu & \left(1_{3 \times 3} - \frac{R_1 R_1^\dagger}{2}\right) \frac{1-S}{\sqrt{2}} R_M^{(1)} & \frac{1+S}{\sqrt{2}} R_M^{(2)} \\ -\frac{R_1^\dagger - R_2^\dagger}{\sqrt{2}} R_\nu & -\frac{1+S}{\sqrt{2}} R_M^{(1)} & \left(1_{3 \times 3} - \frac{R_2 R_2^\dagger}{2}\right) \frac{1-S}{\sqrt{2}} R_M^{(2)} \end{pmatrix} \quad (16)$$

where

$$S = -\frac{1}{4} M^{-1} \mu, \quad R_1 \simeq R_2 \simeq \frac{1}{\sqrt{2}} m_D^* M^{-1} \equiv R \quad (17)$$

The masses of the light active neutrinos are generated via a two-loop inverse seesaw mechanism, with the corresponding mass matrices expressed as follows [13, 17]:

$$\widetilde{M}_\nu = m_D (M^T)^{-1} \mu M^{-1} m_D^T, \quad (18)$$

$$\widetilde{M}_\nu^{(-)} = \frac{1}{2} \mu - \frac{1}{2} (M + M^T), \quad (19)$$

$$\widetilde{M}_\nu^{(+)} = \frac{1}{2} \mu + \frac{1}{2} (M + M^T), \quad (20)$$

The matrix  $\widetilde{M}_\nu$  represents the (predominantly) active neutrino mass matrix, while  $\widetilde{M}_\nu^{(-)}$  and  $\widetilde{M}_\nu^{(+)}$  describe the matrices associated with the exotic neutrino sectors. The resulting physical spectrum consists of three light active neutrinos and four exotic neutrinos, which form two pseudo-Dirac pairs. These pairs have masses approximately given by  $\sim \pm \frac{1}{2} \left( \widetilde{M}_\nu^{(+)} + \left( \widetilde{M}_\nu^{(-)} \right)^T \right)$ , with a small mass splitting  $\mu$  within each pair. The rotation matrix  $R_\nu$ , which diagonalizes the light neutrino mass matrix  $\widetilde{M}_\nu$ , is closely related to the Pontecorvo-Maki-Nakagawa-Sakata (PMNS) matrix  $U_{\text{PMNS}}$ . However, due to mixing between active and heavy exotic neutrinos (encoded in  $R_1$  and  $R_2$ , the PMNS matrix may exhibit slight deviations from unitarity.

We analyzed a benchmark scenario with a diagonal matrix  $M = \text{diag}(M_1, M_2)$  and fitted the effective parameters of the neutrino sector specified in Eqs. (13)-(15) to reproduce the experimental data on  $\Delta m_{i1}^2$  (with  $i = 2, 3$ ) neutrino mass squared differences,  $\sin \theta_{jk}$  ( $j, k = 1, 2, 3, j \neq k$ ) mixing angles, and the CP violating phase  $\delta_{\text{CP}}$ . We randomly varied the parameters of the matrix  $m_D$  between  $[10^{-3}, 1]$ ; for the matrix  $M$  we varied between  $[100, 1000]$  GeV

Benchmark parameters	
$y_{\nu_{11}} = 3.84 \times 10^{-3} e^{0.958i}$	$\mu_{11} = 6.75 \times 10^{-3} e^{-1.35i} \text{ eV}$
$y_{\nu_{12}} = 4.32 \times 10^{-3} e^{-2.02i}$	$\mu_{12} = \mu_{21} = 3.27 \times 10^{-5} e^{-1.33i} \text{ eV}$
$y_{\nu_{21}} = 1.20 \times 10^{-3} e^{-0.623i}$	$\mu_{22} = 2.91 \times 10^{-6} e^{-1.51i} \text{ eV}$
$y_{\nu_{22}} = 9.78 \times 10^{-3} e^{0.846i}$	$M_1 = 6536.9 \text{ GeV}$
$y_{\nu_{31}} = 5.95 \times 10^{-3} e^{-2.42i}$	$M_2 = 531.1 \text{ GeV}$
$y_{\nu_{32}} = 1.23 \times 10^{-2} e^{0.854i}$	

Table II: Effective parameter values for the benchmark point of the model.

whereas for  $\mu$  the range  $[10^{-6}, 10^{-3}] \text{ eV}$  was considered. The phases of  $m_D$  and  $\mu$  were varied in the interval  $[0, 2\pi]$ . The values of the model parameters representing the studied benchmark point are shown in Table II. After performing the fit of the effective parameters and obtaining the benchmark point, we obtained the values shown in Table III, alongside the experimental values of neutrino oscillation parameters within the  $1\sigma$  and  $3\sigma$  ranges, as reported in Refs. [56, 57]. In Table III, we see that the neutrino mass-squared differences ( $\Delta m_{21}^2$ ,  $\Delta m_{31}^2$ ) and the solar and reactor mixing angles ( $\sin^2 \theta_{12}^{(l)}$ ,  $\sin^2 \theta_{13}^{(l)}$ ) lie within the  $1\sigma$  range. The atmospheric mixing angle ( $\sin^2 \theta_{23}^{(l)}$ ) and the leptonic Dirac CP-violating phase ( $\delta_{\text{CP}}$ ) are within the  $2\sigma$  range.

Furthermore, our model can predict the effective Majorana neutrino mass parameter of the neutrinoless double beta decay ( $0\nu\beta\beta$ ), which gives us information about the Majorana nature of neutrino. This observable depends on the mixing parameters and the masses of the light-active neutrinos as follows,

$$m_{ee} = \left| \sum_i \mathbf{U}_{ei}^2 m_{\nu i} \right|, \quad (21)$$

where  $\mathbf{U}_{ei}$  and  $m_{\nu i}$  are the matrix elements of the PMNS leptonic mixing matrix and the light active neutrino masses, respectively. From the equation (21), we can see that the neutrinoless double beta ( $0\nu\beta\beta$ ) decay amplitude is proportional to  $m_{ee}$ .

Figures 2a and 2b show the correlation between the effective mass parameter  $m_{ee}$  of  $0\nu\beta\beta$ , the CP violation phase and the mixing angle  $\sin^2 \theta_{12}$  for different values of the mixing angle  $\sin^2 \theta_{13}$  and  $\sin^2 \theta_{13}$ , respectively. The red background fringe represent the  $1\sigma$  range of the experimental values and the black dotted lines represent our benchmark point for each observable. In Figure 2, we see that for the mixing angles and the CP violating phase, we obtain values up to  $3\sigma$ , where each lepton sector observable is obtained in the following range of values:  $0.532 \lesssim \sin^2 \theta_{23} \lesssim 0.616$ ,  $0.0201 \lesssim \sin^2 \theta_{13} \lesssim 0.0241$ ,  $0.27 \lesssim \sin^2 \theta_{12} \lesssim 0.366$  and  $128 \lesssim \delta_{\text{CP}} \lesssim 260$ .

Therefore, assuming normal neutrino mass hierarchy, one finds that the Majorana neutrino mass parameter is bounded to be in the range  $2.14 \text{ meV} \lesssim m_{ee} \lesssim 4.39 \text{ meV}$ . This region is clearly shown in Figure 2, where all values are below the current experimental limit. The current most stringent experimental upper bound on the effective Majorana neutrino mass parameter, i.e.,  $m_{ee} < (28 - 122) \text{ meV}$  (90% C.L.), arises from the KamLAND-Zen limit on the  $^{136}\text{Xe}$   $0\nu\beta\beta$  decay half-life  $T_{1/2}^{0\nu\beta\beta}(^{136}\text{Xe}) > 3.8 \times 10^{26} \text{ yr}$  (90% C.L.) [58].

## V. DARK MATTER

Due to the preserved  $Z_3$  symmetry, our model contains stable scalar and fermionic dark matter candidates, whose stability is ensured by this discrete symmetry. The dark matter candidate corresponds to the lightest electrically neutral particle transforming non-trivially under the preserved  $Z_3$  symmetry.

Depending on the mass hierarchy among the new particles, either a scalar or a fermionic dark matter scenario can be

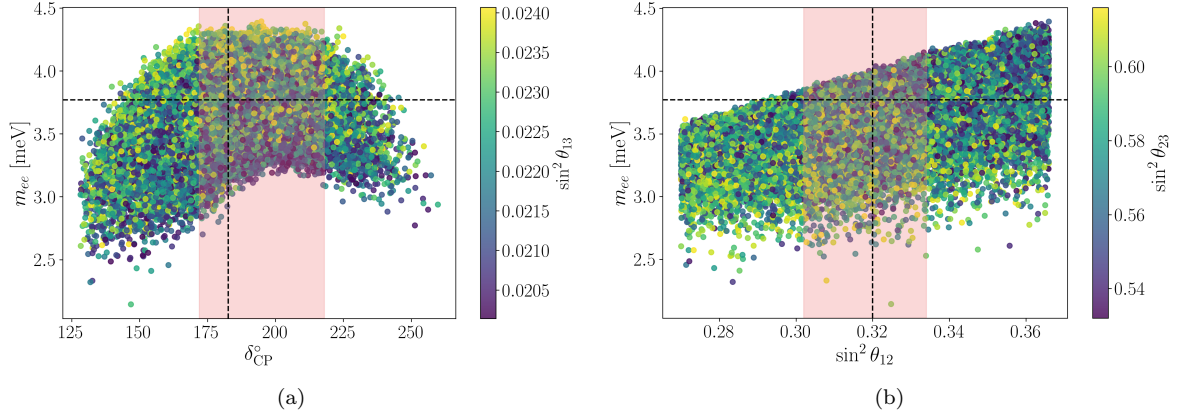


Figure 2: Correlation plot between the effective mass parameter of the neutrinoless double beta decay ( $0\nu\beta\beta$ )  $m_{ee}$  and a) CP violation phase  $\delta_{CP}^{(l)}$ , for different values of the mixing angle  $\sin^2 \theta_{13}$  and b) for the mixing angle  $\sin^2 \theta_{12}$  and different values of the mixing angle  $\sin^2 \theta_{13}$ .

Observable	range	$\Delta m_{21}^2$ [ $10^{-5}\text{eV}^2$ ]	$\Delta m_{31}^2$ [ $10^{-3}\text{eV}^2$ ]	$\sin^2 \theta_{12}^{(l)}/10^{-1}$	$\sin^2 \theta_{13}^{(l)}/10^{-2}$	$\sin^2 \theta_{23}^{(l)}/10^{-1}$	$\delta_{CP}^{(l)}(^{\circ})$
Experimental	$1\sigma$	$7.50^{+0.22}_{-0.20}$	$2.55^{+0.02}_{-0.03}$	$3.18 \pm 0.16$	$2.200^{+0.069}_{-0.062}$	$5.74 \pm 0.14$	$194^{+24}_{-22}$
Value [56]	$3\sigma$	$6.94 - 8.14$	$2.47 - 2.63$	$2.71 - 3.69$	$2.000 - 2.405$	$4.34 - 6.10$	$128 - 359$
Experimental	$1\sigma$	$7.49 \pm 0.19$	$2.513^{+0.021}_{-0.019}$	$3.08^{+0.12}_{-0.11}$	$2.215^{+0.058}_{-0.056}$	$4.7^{+0.17}_{-0.13}$	$212^{+26}_{-41}$
Value [57]	$3\sigma$	$6.92 - 8.05$	$2.451 - 2.578$	$2.75 - 3.45$	$2.03 - 2.388$	$4.35 - 5.85$	$124 - 364$
Fit	$1\sigma - 3\sigma$	7.69	2.54	3.41	2.24	5.73	219.7

Table III: Numerical Results for the Normal-Ordering (NO) neutrino-mass scenario.

realized. *Scalar dark matter scenario:* This occurs when  $m_\rho < m_\Omega$ , with the  $\rho$ -singlet as the dark matter candidate. In this regime, the decay channel  $\Omega \rightarrow N\rho$  is kinematically accessible (see Figure 3). *Fermionic dark matter scenario:* This is realized when  $m_\rho > m_\Omega$ . Here,  $\Omega$  acts as a fermionic dark matter candidate. In this case, we consider a benchmark scenario where  $m_\Omega > 2m_N$  in order to kinematically open the DM annihilation channel  $\Omega\Omega \rightarrow NN$ , which is crucial to successfully reproduce the experimentally measured amount of dark matter relic abundance.

In this section, we analyze the implications of our model for both scalar and fermionic dark matter scenarios, taking into account the experimentally allowed range for the dark matter relic abundance measured by the Planck collaboration [59]:

$$\Omega h^2 = 0.1200 \pm 0.0012. \quad (22)$$

We will also address the compatibility of our model with the direct DM detection experiments XENON1T [60], XENONnT [61], LUX-ZEPLIN [62] and DARWIN [63] deriving the corresponding constraints on the model parameter space.

### A. Scalar dark matter

The physical masses for the CP even ( $\rho_R$ ) and CP odd ( $\rho_I$ ) components of the  $\rho$ -singlet are degenerate, as seen in section III. Therefore, we consider the SM singlet  $\rho$  a viable complex scalar DM candidate with mass  $m_\rho$  as given in (5) and satisfying  $m_\Omega > m_\rho$ . In this scenario, the decay channels  $\rho \rightarrow \Omega N$  and  $\rho \rightarrow \Omega\Omega$  are forbidden, making the  $\rho$ -scalar stable as required for a DM candidate. The mixing of  $\rho$  with the Higgs boson, arising after electroweak

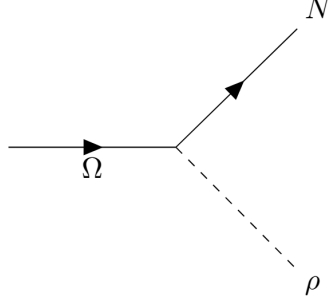


Figure 3: Feynman diagram for the  $\Omega$  decay into the  $\rho$ -singlet and the fermion  $N$ .

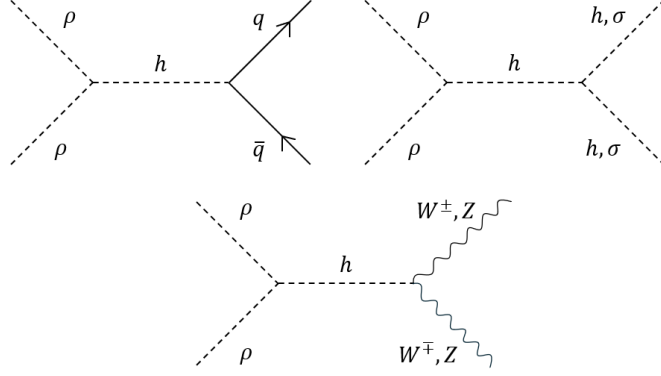


Figure 4: Some Feynman diagrams contributing to  $\rho\rho$  annihilation to SM particles.

symmetry breaking, contributes to dark matter annihilation by enabling  $s$ -channel processes mediated by the CP-even component of the Higgs field (see Figure 4). The list of annihilation cross sections relevant for the  $\rho$ -DM candidate scenario is

$$v_{\text{rel}}\sigma(\rho\rho \rightarrow WW) = \frac{\lambda_{\phi\rho}^2}{8\pi} \frac{s \left(1 + \frac{12m_W^4}{s^2} - \frac{4m_W^2}{s}\right)}{(s - m_h^2)^2 + m_h^2\Gamma_h^2} \sqrt{1 - \frac{4m_W^2}{s}}, \quad (23)$$

$$v_{\text{rel}}\sigma(\rho\rho \rightarrow ZZ) = \frac{\lambda_{\phi\rho}^2}{16\pi} \frac{s \left(1 + \frac{12m_Z^4}{s^2} - \frac{4m_Z^2}{s}\right)}{(s - m_h^2)^2 + m_h^2\Gamma_h^2} \sqrt{1 - \frac{4m_Z^2}{s}}, \quad (24)$$

$$v_{\text{rel}}\sigma(\rho\rho \rightarrow q\bar{q}) = \frac{N_c\lambda_{\phi\rho}^2 m_q^2}{4\pi} \frac{\left(1 - \frac{4m_q^2}{s}\right)^{3/2}}{(s - m_h^2)^2 + m_h^2\Gamma_h^2}, \quad (25)$$

$$v_{\text{rel}}\sigma(\rho\rho \rightarrow hh) = \frac{\lambda_{\phi\rho}^2}{16\pi s} \left[1 + \frac{3m_h^2}{s - m_h^2} - \frac{4\lambda_{\phi\rho}v^2}{s - 2m_h^2}\right]^2 \sqrt{1 - \frac{4m_h^2}{s}}, \quad (26)$$

$$v_{\text{rel}}\sigma(\rho\rho \rightarrow \sigma\sigma) = \frac{\sqrt{s - 4m_\sigma^2}}{8\pi s^{\frac{3}{2}}} \left[ \frac{v_\phi^4 \lambda_{\phi\rho}^2 \lambda_{\phi\sigma}^2}{(s - m_h^2)^2 + m_h^2\Gamma_h^2} + \frac{2(s - m_h^2)v_\phi^2 \lambda_{\phi\rho} \lambda_{\phi\sigma} \lambda_{\sigma\rho}}{(s - m_h^2)^2 + m_h^2\Gamma_h^2} + \lambda_{\sigma\rho}^2 \right] \quad (27)$$

where  $\sqrt{s}$  is the center-of-mass energy,  $N_c = 3$  is the color factor,  $m_h = 125.7 \text{ GeV}$  and  $\Gamma_h = 4.1 \text{ MeV}$  are the SM Higgs boson  $h$  mass and its total decay width, respectively. The final-state  $q\bar{q}$  stands for  $t$  and  $b$  quarks.

Below, in our analysis we neglect the  $v^2$  dependent terms.

### 1. Direct Detection

The spin-independent cross section for the  $\rho$ -nucleon elastic scattering is dominated by the contribution shown in Figure 5. It is induced by the same Higgs portal interaction as in the  $\rho - \rho$  annihilation, resulting in the well-known correlation between these observables. For this contribution, the total cross section is given by [64]

$$\sigma_{SI} = \frac{f_n^2 m_n^4 \lambda_{\phi\rho}^2}{8\pi m_h^4 m_\rho^2}; \quad (28)$$

Here,  $m_n$  is the nucleon mass and  $f_n \simeq 1/3$  corresponds to the form factor [65, 66]. We derive constraints on the  $\rho$ -DM scenario by comparing the above expression with the latest limits on  $\sigma_{SI}$  from XENON1T [67], XENONnT [68], and the projected sensitivity of LUX-ZEPLIN [69] and DARWIN [70].

We focus on the region of parameter space where  $\lambda_{\phi\rho} \lesssim 1$ ,  $\lambda_{\sigma\rho} \neq 0$ ,  $\lambda_{\phi\sigma} \neq 0$ ,  $0.8 \text{ TeV} \lesssim m_\Omega \lesssim 2.0 \text{ TeV}$ , and  $1 \text{ TeV} \lesssim m_\rho \lesssim 3.0 \text{ TeV}$ . Within this region, relic density saturation is achieved, as indicated by the points in Figure 6 (a) and (b). Interestingly, values of  $\lambda_{\phi\rho} \gtrsim 0.5$  are entirely excluded across the full dark matter mass range. Moreover, only values  $\lambda_{\phi\rho} \lesssim 0.1$  can avoid the projected limits from XENONnT (20 ton-year) and DARWIN (200 ton-year), even in the case of sub-abundant dark matter. Furthermore, Figure 7 (a) shows more clearly that, in order to elude a large spin-independent scattering cross section, it is necessary to increase the dark matter mass, which in turn tends to bring the model closer to relic density saturation.

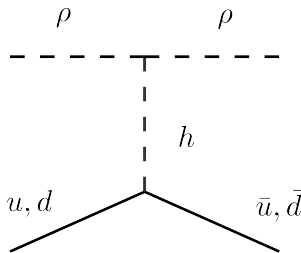


Figure 5: Feynman diagram for the dark matter contribution to spin-independent direct detection at tree-level.

On the other hand, the mass of the dark matter candidate does not appear to be excluded by current experiments, allowing for values in the range  $1 \text{ TeV} \lesssim m_\rho \lesssim 2.8 \text{ TeV}$ . However, a heavier  $\rho$ -singlet can more easily escape the direct detection bounds and saturate the measured relic density, as shown in Figure 7 (b). In contrast, lighter  $\rho$  masses exhibit larger spin-independent cross sections, even when  $\Omega h^2 \simeq 0.12$ . Meanwhile, the mass of the  $\sigma$ -singlet appears to play a minor role in the allowed parameter space, although the plots indicate that it typically falls below 1.8 TeV for relic density saturation and below 1.6 TeV for sub-abundant dark matter.

Additionally, another possible scenario arises when the  $\rho$ -singlet is lighter than the  $\sigma$ -singlet, effectively this closes the annihilation channel  $\rho\rho \rightarrow \sigma\sigma$ . While this configuration is viable in principle, it presents significant phenomenological challenges. This will suppress the total average annihilation cross sections pushing the relic density to generate it's overabundance. Moreover reducing the  $\rho$ -singlet mass due to this scenario, typically enhances the spin-independent scattering cross section, making the scenario increasingly constrained by the XENON1T and LUX-ZEPLIN experiments. Taken together, these effects render this benchmark less favored in light of current experimental bounds.

### 2. Indirect Detection

In the previous sub-section, we discussed the challenges faced by the model in producing observable signals in direct detection experiments. We emphasized that the coupling  $\lambda_{\rho\phi}$  plays a crucial role in connecting the dark matter

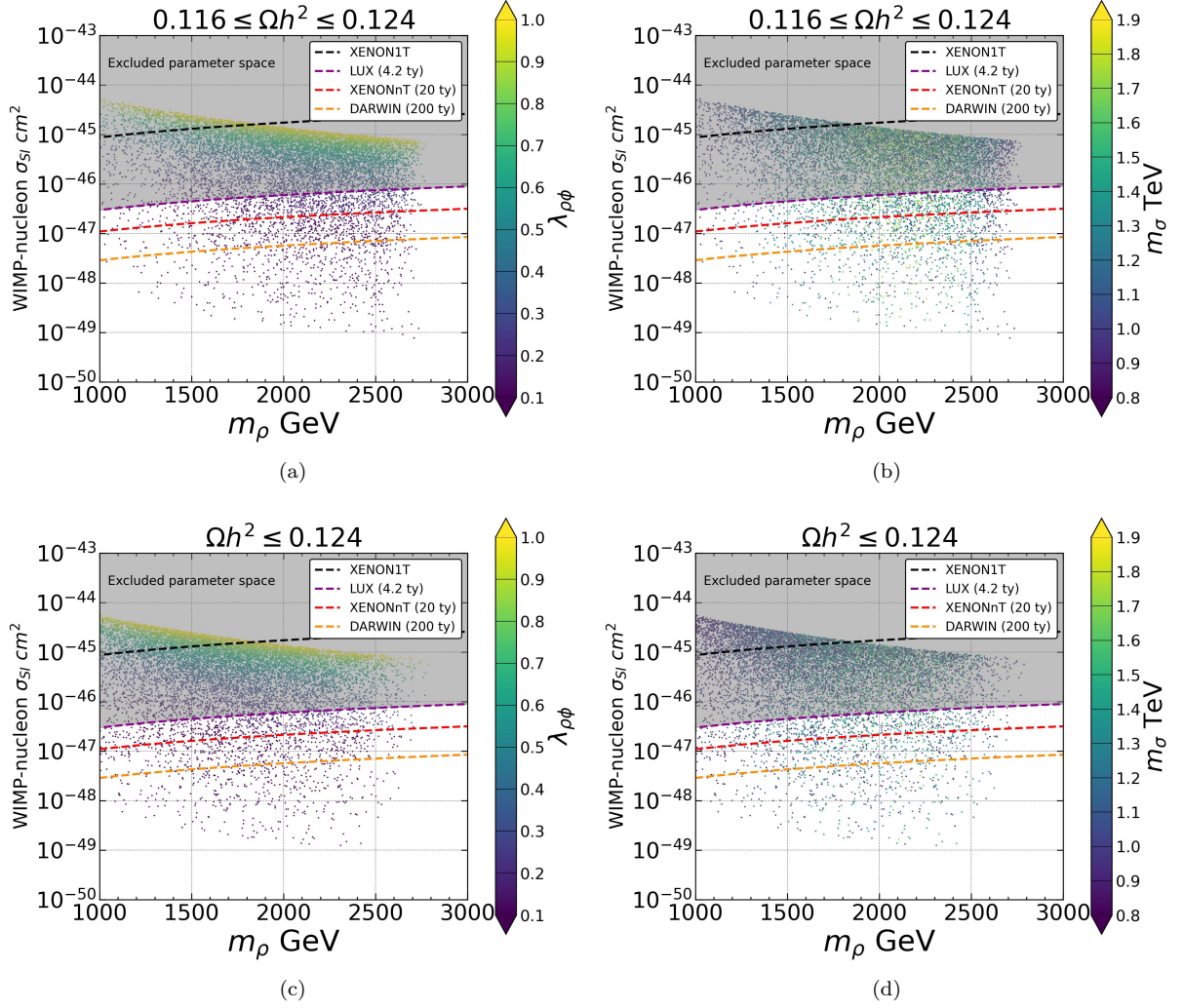


Figure 6: Spin-independent elastic DM-nucleon scattering cross section as a function of the DM mass. The gray area represents the excluded parameter space given by the XENON1T and LUX-ZEPLIN at 4.2 ton-year represented by the black and purple lines respectively. While the red line shows the future projections from XENONnT at 20 ton-year and the orange line the projections for DARWIN at 200 ton-year. Points in plots (a) and (b) satisfy the relic density saturation constraint within  $3\sigma$ , whereas plots (c) and (d) correspond to sub-abundant dark matter scenarios. The color map in (a) and (c) indicates the  $\rho$ -Higgs coupling, while in (b) and (d) it represents the mass of the  $\sigma$ -singlet.

particles to the Standard Model sector via the Higgs boson, effectively acting as a Higgs portal. This interaction not only affects the spin-independent DM-nucleon cross section, but also governs the dominant annihilation channels of the dark matter candidate. In particular, we focused on the annihilation cross sections  $\langle\sigma v\rangle_{\rho\rho\rightarrow b\bar{b}}$  and  $\langle\sigma v\rangle_{\rho\rho\rightarrow W+W^-}$ , where the most stringent current bounds on weak-scale DM annihilation are given in [71].

We observe in both plots of Figure 8 a small region excluded by current experimental bounds, specifically due to the annihilation channel with  $b\bar{b}$  in the final state. Even when considering both relic density saturation and sub-abundant dark matter, the viable parameter space is limited to values around  $m_\rho \lesssim 1.1$  TeV and  $\lambda_{\rho\phi} \sim 1$ , the latter already ruled out by direct detection constraints. Conversely, the annihilation cross section  $\langle\sigma v\rangle_{\rho\rho\rightarrow b\bar{b}}$  remains sufficiently suppressed to evade current experimental sensitivity.

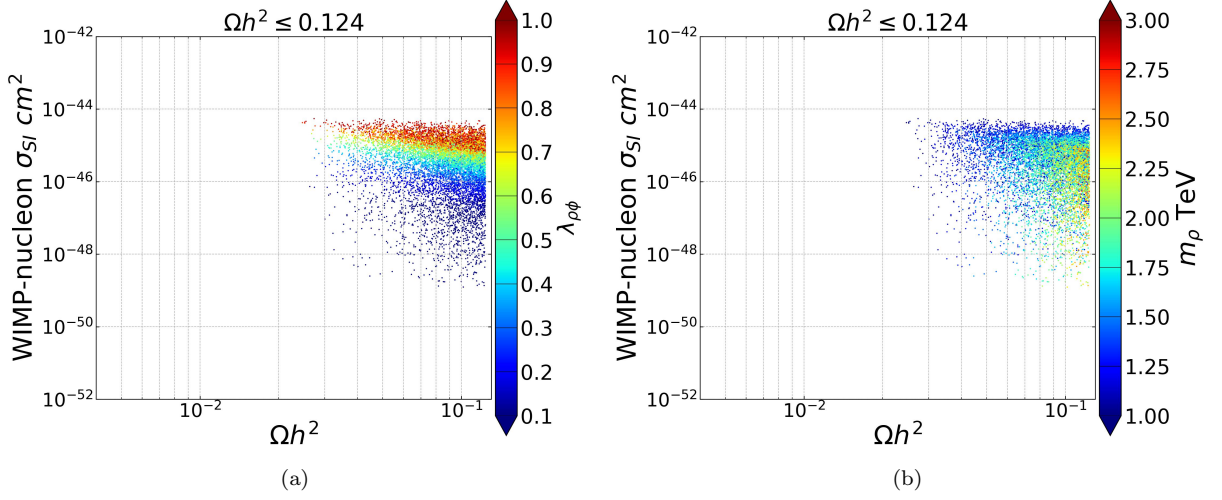


Figure 7: Spin-independent elastic DM-nucleon scattering cross section as a function of the relic density. The color map represents the  $\rho$ -Higgs coupling and the mass of the DM in (a) and (b) respectively.

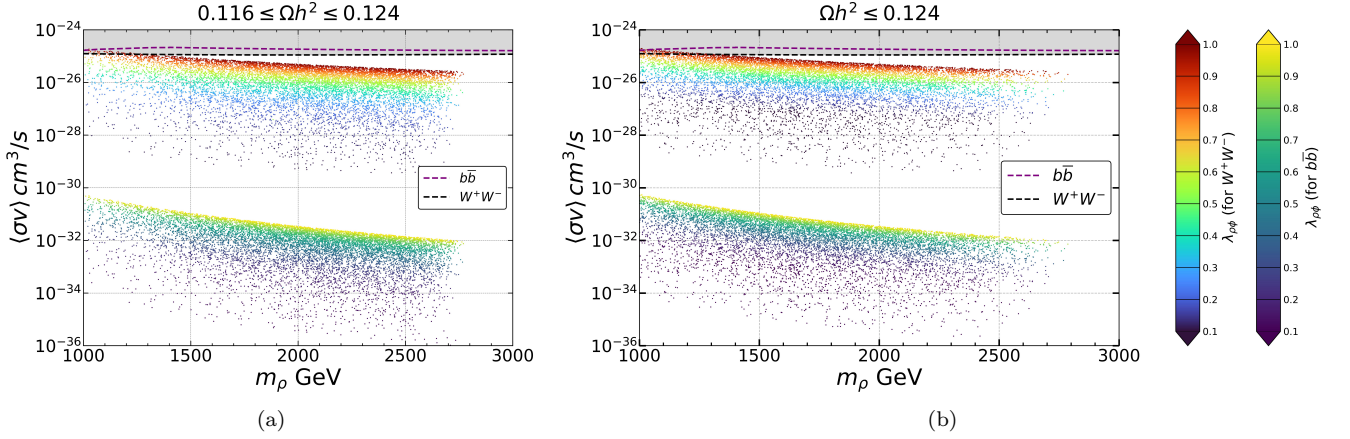


Figure 8: Thermally averaged total annihilation cross-section as a function of the DM mass. Both color maps represent the  $\rho$ -Higgs coupling  $\lambda_{\rho\phi}$ , the left one is for the annihilation cross-section with  $W^+W^-$  as final states, while the right one is with  $b\bar{b}$ . The dashed purple and black lines represent the experimental limits for the annihilation cross-sections taken from Ref. [71]. All the points in the graph (a) satisfy the relic density saturation constraint within  $3\sigma$ , whereas in the graph (b) correspond to sub-abundant dark matter.

## B. Fermionic dark matter

As mentioned, the model also admits a *fermionic* dark-matter candidate. This happens when  $\Omega$  is the lightest  $Z_3$ -nontrivial state. In practice we consider  $m_\Omega < m_\rho$ , which ensures  $\Omega$ 's stability under the exact  $Z_3$  symmetry. The process that maintains  $\Omega$  in thermal equilibrium with the primordial plasma is  $\Omega\bar{\Omega} \rightarrow N\bar{N}$ , mediated by a  $t$ -channel exchange of the SM-singlet scalar  $\rho$ , as shown in Fig. 9. The final state contains the lightest sterile neutrinos  $N$  introduced in Sec. IV.

The corresponding thermally averaged cross section is given by [72]

$$\langle\sigma v\rangle\simeq\frac{y_N^4m_\Omega^2\sqrt{1-\frac{4m_N^2}{m_\Omega^2}}}{32\pi\left(m_\rho^2+m_\Omega^2-m_N^2\right)^2},\quad(29)$$

where the  $y_N$  is the  $\Omega N\rho$  Yukawa coupling introduced in (11).

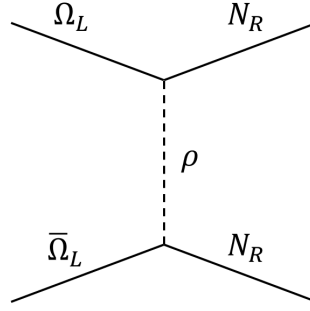


Figure 9: Feynman diagram for the DM  $\Omega$  annihilation to the sterile neutrino.

### 1. Direct Detection

Unlike the previous case of the scalar DM candidate  $\rho$ , the fermionic DM candidate  $\Omega$  does not receive any tree-level contribution to its scattering off nuclei, since  $\rho$ - $h$  mixing is forbidden in our model. The process responsible for the DM direct detection is therefore dominated by the one-loop penguin diagrams shown in Fig. 10. As a result, it is loop-suppressed with respect to  $\Omega\Omega$  annihilation, which is determined by the tree-level diagram in Fig. 9. This allows for the reconciliation of the stringent direct-detection constraints and the observable relic density. The corresponding contribution to the spin-independent scattering cross section is given by [73]

$$\sigma_{SI}=\left(\frac{m_n}{v}\right)^2\frac{(\mu_{DM-n})^2}{\pi m_h^4}f_n^2\left(\sum_{i=1}^3g_{\Omega\Omega h,i}\right)^2,\quad(30)$$

where  $\mu_{DM-n}=\frac{M_{DM}m_n}{M_{DM}+m_n}$  is the reduced mass of DM-nucleon system with  $m_n$  being the mass of the nucleon in GeV and  $f_n=0.3$  [74]. The effective coupling  $g_{\Omega\Omega h}$  between DM and Higgs is given by

$$\begin{aligned} g_{\Omega\Omega h,1}&=\frac{\lambda_{\rho\phi}vy_N^2m_N\left((m_\rho^2-m_N^2)+m_\rho^2\ln\left(\frac{m_N^2}{m_\rho^2}\right)\right)}{8\pi^2(m_\rho^2-m_N^2)^2} \\ g_{\Omega\Omega h,2}&=\frac{\lambda_{\rho\phi}vz_\Omega^2m_\Omega\left((m_\rho^2-m_\Omega^2)+m_\rho^2\ln\left(\frac{m_\Omega^2}{m_\rho^2}\right)\right)}{8\pi^2(m_\rho^2-m_\Omega^2)^2} \\ g_{\Omega\Omega h,3}&=\frac{\lambda_{\sigma\phi}vy_\Omega^2m_\Omega\left((m_\sigma^2-m_\Omega^2)+m_\sigma^2\ln\left(\frac{m_\Omega^2}{m_\sigma^2}\right)\right)}{8\pi^2(m_\sigma^2-m_\Omega^2)^2} \end{aligned}$$

The spin-independent DM-nucleon scattering cross section is shown in Fig. 11 as a function of the dark matter candidate mass. The relic density saturation is achieved. Plot 11a shows that almost all points are below the parameter space excluded by current experiments, in the mass range  $1.0\text{ TeV}\lesssim m_\Omega\lesssim 5.0\text{ TeV}$  and also it is shown a

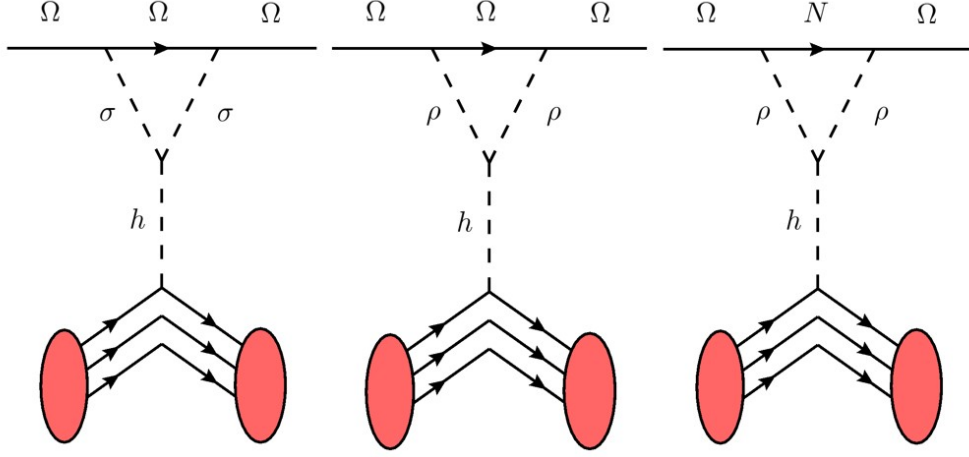


Figure 10: Penguin diagrams for the dark matter contribution to spin-independent direct detection via one-loop process.

correlation between the mass of the DM candidate and the mass of the scalar singlet  $\rho$  indicating that the larger the masses, the smaller the spin-independent cross section. In plot 11b we obtain a similar behavior between DM mass and the spin-independent cross section in the same mass range but with no apparent correlation with the other scalar singlet  $\sigma$ .

In Fig.12a we can observe the mass of the heavy sterile neutrinos versus the mass of the fermionic DM. In the range of 1 – 2 TeV for the  $m_\Omega$ , it is possible to observe that as the mass of the heavy neutrinos increases, their quantity decreases, making it so that for  $m_\Omega = 2$  TeV there are practically no mass values of heavy neutrinos close to 1 TeV. However, it is also possible to observe that from  $m_\Omega = 2$  TeV onward, there is a direct correlation with the mass of the scalar mediator  $\rho$ , that is, as the  $m_\Omega$  increases, so does the  $m_\rho$ .

In Fig.12b, we plot the neutrino Yukawa coupling  $Y_N$  versus the  $m_\Omega$ . We take a range of values for  $Y_N$  between 1.5 – 3.5 where we can see that this coupling is strongly restricted by the  $m_\Omega$ . For example, for values of  $m_\Omega = 2$  TeV,  $Y_N$  can take values between 2.0 and 3.5, but if we increase the omega mass to  $m_\Omega = 4$  TeV,  $Y_N$  can only take values between 3.0 and 3.5. However, as in the plot 12b,  $m_\Omega$  is directly correlated with  $m_\rho$ . This analysis establishes a lower bound for the omega mass since below 1000 GeV it is not possible to obtain a Yukawa coupling.

## VI. CHARGED LEPTON FLAVOR VIOLATION

Now, we will study the charged lepton flavor violation processes due to the mixing between the light active and heavy sterile neutrino of the model. The branching ratio for the one-loop decay  $l_i \rightarrow l_j \gamma$  is given by [75, 76]:

$$\text{BR}(l_i \rightarrow l_j \gamma) = \frac{\alpha_W^3 s_W^2 m_{l_i}^5}{256 \pi^2 m_W^4 \Gamma_i} |G_{ij}|^2, \quad (31)$$

where  $\Gamma_\mu = 3 \times 10^{-19}$  GeV is the total muon decay width and  $G_{ij}$  has the following structure,

$$G_{ij} \simeq \sum_{k=1}^3 \left( [(1 - RR^\dagger) U_\nu]^* \right)_{ik} ((1 - RR^\dagger) U_\nu)_{jk} G_\gamma \left( \frac{m_{\nu_k}^2}{m_W^2} \right) + 2 \sum_{l=1}^2 (R^*)_{il} (R)_{jl} G_\gamma \left( \frac{m_{N_{Rl}}^2}{m_W^2} \right), \quad (32)$$

$$G_\gamma(x) = \frac{10 - 43x + 78x^2 - 49x^3 + 18x^3 \ln x + 4x^4}{12(1-x)^4}.$$

Here,  $U_\nu$  is the matrix that diagonalizes the light active neutrino, and since we are considering the diagonal charged lepton mass matrix, we have that  $U_{\text{PMNS}} = U_l^\dagger U_\nu = U_\nu$  (since  $U_l = \mathbb{I}$ ), while the matrix  $R$  is a rotation matrix given

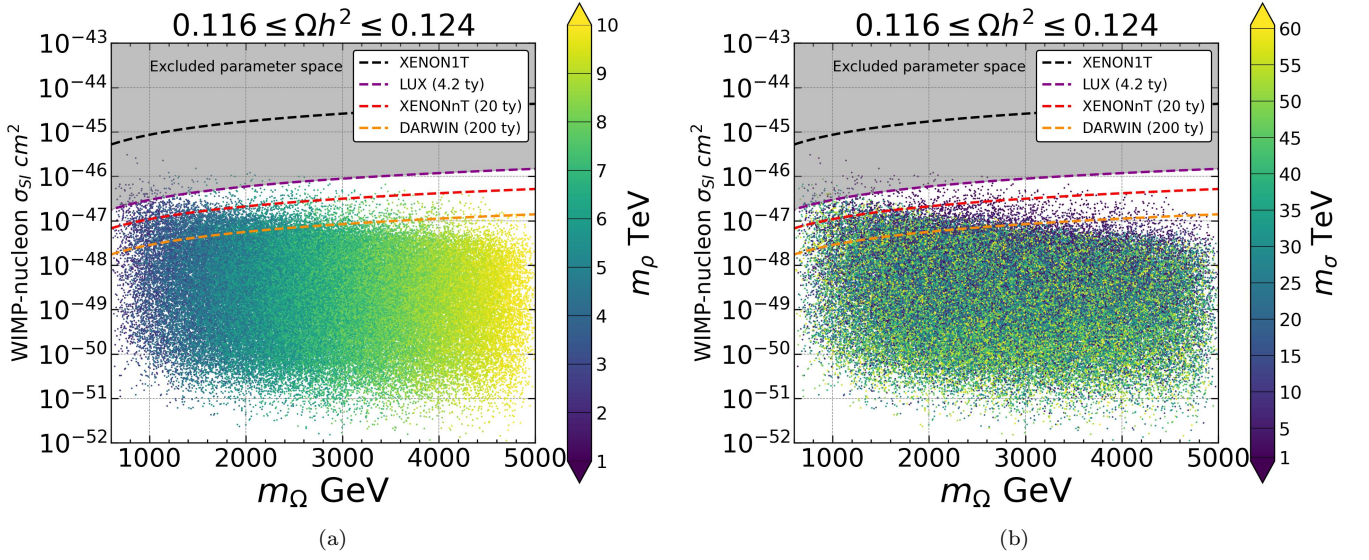


Figure 11: Spin-independent elastic DM-nucleon scattering cross section as a function of the DM mass. All the points satisfied the saturation of relic density at  $3\sigma$ . The color map indicates the mass of the  $\rho$  singlet. The gray area represents the excluded parameter space given by the XENON1T and LUX-ZEPLIN at 4.2 ton-year represented by the black and purple lines respectively. While the red line shows the future projections from XENONnT at 20 ton-year and the orange line the projections for DARWIN at 200 ton-year.

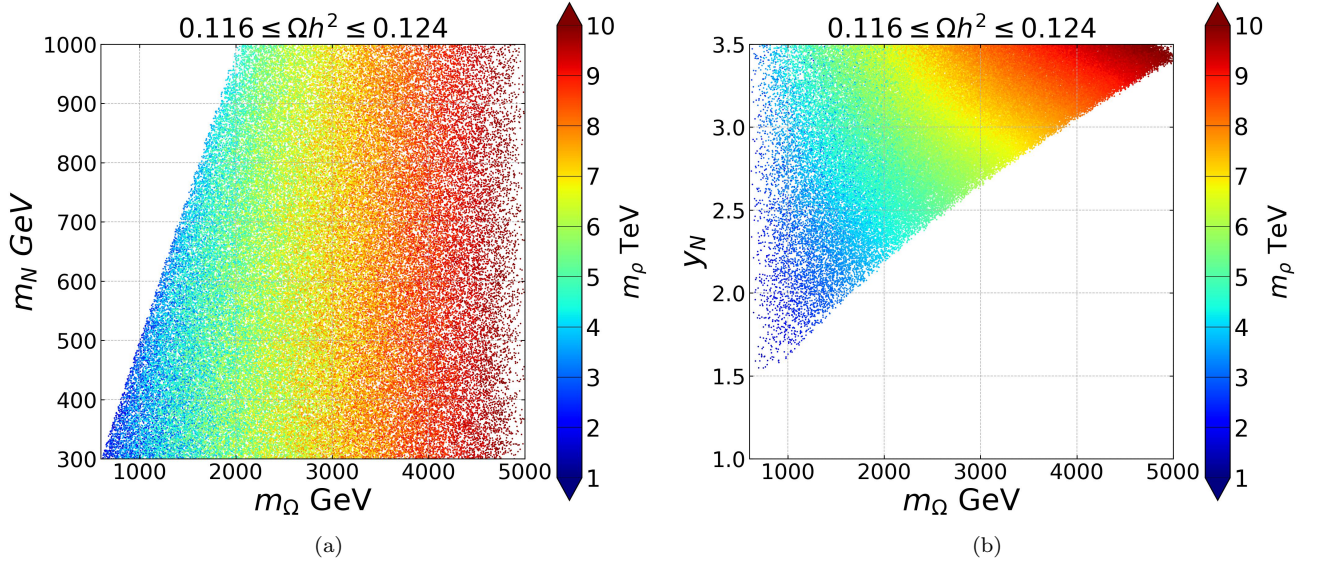


Figure 12: (a) Mass of the sterile heavy neutrino as a function of the DM mass and (b) Neutrino Yukawa coupling  $y_N$  as a function of the DM mass. All the points satisfied the saturation of relic density at  $3\sigma$ . The color map indicates the mass of the  $\rho$  singlet.

by,

$$R = \frac{1}{\sqrt{2}} m_D^* M^{-1}, \quad (33)$$

where  $M$  and  $m_D$  are the same matrices of the Eq. (13).

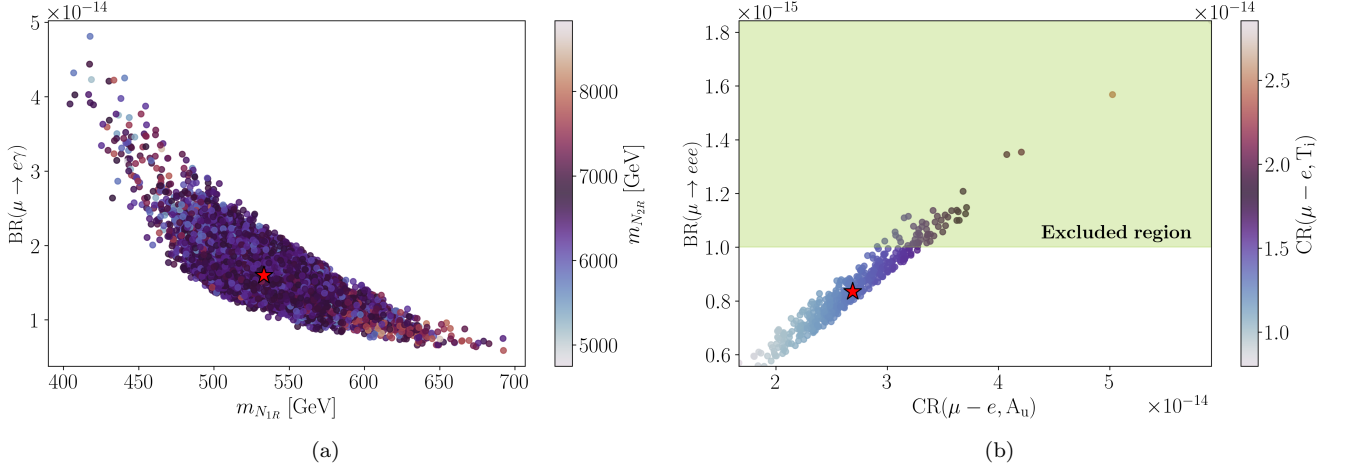


Figure 13: a) Scatter plot between the branching ratio of the process  $\mu \rightarrow e\gamma$  and the mass of the lightest Majorana neutrino, considering different values of the mass of the heaviest Majorana neutrino. b) Scatter plot between the branching ratio of the process  $\mu \rightarrow eee$  and  $\text{CR}(\mu - e, A_u)$ , considering different values of the  $\text{CR}(\mu - e, T_i)$

Our model predicts values below the experimental limit for the process  $\mu \rightarrow e\gamma$ , whose value according to the MEG II collaboration is equal to [77],

$$\text{BR}(\mu \rightarrow e\gamma)_{\text{exp}} \leq 1.5 \times 10^{-13}, \quad (34)$$

while the value for the benchmark point of the model according to the equation Eq. (31) corresponds to,

$$\text{BR}(\mu \rightarrow e\gamma) \simeq 1.6 \times 10^{-14} \quad (35)$$

In Fig. 13a, a scatter plot is shown between the Branching ratio for the  $\mu \rightarrow e\gamma$  process versus the mass of the lightest sterile right neutrino ( $m_{N_1}$ ), in relation to the different values of the mass of the heaviest sterile right neutrino ( $m_{N_2}$ ). This plot was generated by perturbing the benchmark point around 20% and placing a restriction that each generated point is in agreement with the experimental values of the neutrino oscillation (see Table III), representing the benchmark point of the model with the star point (red), where the value for the masses of sterile right neutrino are  $m_{N_1} \lesssim 533.1$  GeV and  $m_{N_2} \lesssim 6537$  GeV. In addition, we can see that each point in the plot is below the experimental limit according to the MEG II collaboration, for the mass range for the lightest right neutrino between approximately 400 GeV  $\lesssim m_{N_1} \lesssim 700$  GeV. In turn, we can also see that the model predicts masses for the heaviest right neutrino in the 4750 GeV  $\lesssim m_{N_2} \lesssim 8800$  GeV range.

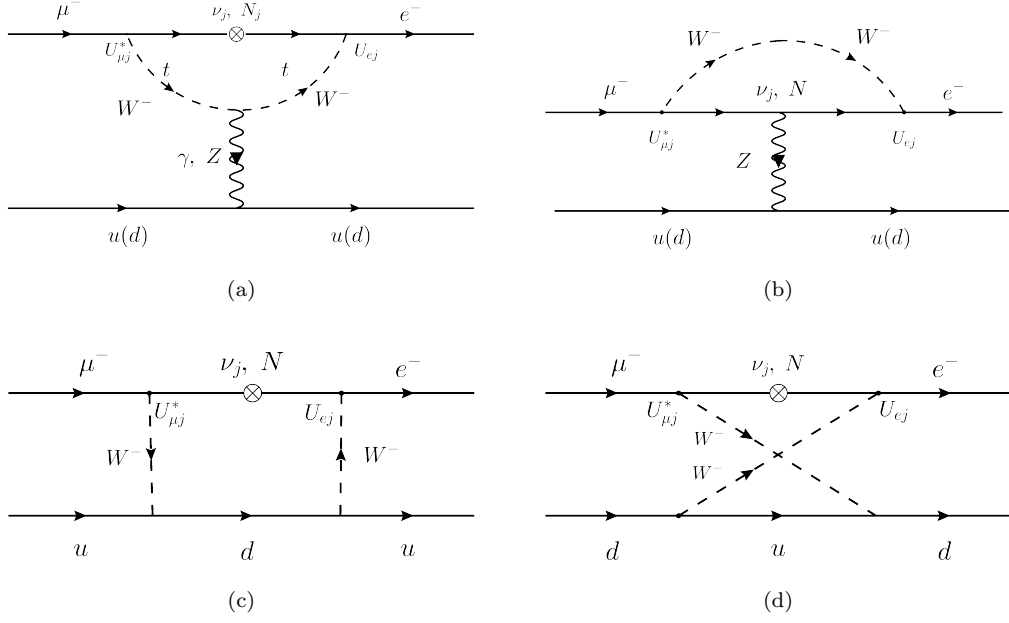
#### A. $\text{CR}(\mu - e, N)$

The  $\mu - e$  conversion refers to the decay of a muon bound to an atom, that is, when an atom captures a muon (muon atom), falling to the first state of a target nucleus N without neutrino emission. The conversion rate is defined as

$$\text{CR}(\mu - e, N) \equiv \frac{\Gamma(\mu^- + N \rightarrow e^- + N)}{\Gamma(\mu^- + N \rightarrow \text{all})} \quad (36)$$

Box and penguin diagrams of Fig. 14 contribute as[41],

$$\text{CR}(\mu - e, N) = \frac{2G_F^2 \alpha_w^2 m_\mu^5}{(4\pi)^2 \Gamma_{\text{capt}}(Z)} \left| 4V^{(p)} \left( 2\tilde{F}_u^{\mu e} + \tilde{F}_d^{\mu e} \right) + 4V^{(n)} \left( \tilde{F}_u^{\mu e} + 2\tilde{F}_d^{\mu e} \right) + DG_\gamma^{\mu e} \frac{s_w^2}{2\sqrt{4\pi\alpha}} \right|^2 \quad (37)$$

Figure 14: Penguin diagrams for  $\mu - e$  conversion.

where  $\Gamma_{\text{capt}(Z)}$  denotes the capture rate of a nucleus with atomic number  $Z$  [78],  $G_F$  is the Fermi constant,  $m_\mu$  the muon mass,  $\alpha = e^2/(4\pi)$ , with  $s_w$  corresponding to the sine of the weak mixing angle. The form factors  $\tilde{F}_q^{\mu e}$  ( $q = u, d$ ) are given by

$$\tilde{F}_d^{\mu e} = Q_q s_w^2 F_\gamma^{\mu e} + F_Z^{\mu e} \left( \frac{I_q^3}{2} - Q_q s_w^2 \right) + \frac{1}{4} F_{\text{box}}^{\mu e q q}, \quad (38)$$

where  $Q_q$  denotes the quark electric charge ( $Q_u = 2/3$ ,  $Q_d = -1/3$ ) and  $I_q^3$  is the weak isospin ( $I_u^3 = 1/2$ ,  $I_d^3 = -1/2$ ). The quantities  $F_\gamma^{\mu e}$ ,  $F_Z^{\mu e}$  and  $F_{\text{box}}^{\mu e q q}$  correspond to the different form factors of the diagrams, and  $G_\gamma^{\mu e}$  corresponds to the dipole term; all expressions are in ref. [41]. The relevant nuclear information (nuclear form factors and averages over the atomic electric field) is encoded in the form factors D, V (p), and V (n). In our analysis, we use the numerical values presented in ref. [78].

### B. $\ell_\alpha \rightarrow \ell_\beta \ell_\beta \ell_\rho$

Next, we will see the analysis for the branching ratio of the muon decaying to three electrons, where according to [79, 80], it is given by:

$$\begin{aligned} \text{BR}(\mu \rightarrow eee) = & \frac{\alpha_w^4}{24576\pi^3} \frac{m_\mu^4}{M_W^4} \frac{m_\mu}{\Gamma_\mu} \times \left\{ 2 \left| \frac{1}{2} F_{\text{Box}}^{\mu e e e} + F_Z^{\mu e} - 2s_w^2 (F_Z^{\mu e} - F_\gamma^{\mu e}) \right|^2 + 4s_w^4 |F_Z^{\mu e} - F_\gamma^{\mu e}|^2 \right. \\ & + 16s_w^2 \text{Re} \left[ (F_Z^{\mu e} + \frac{1}{2} F_{\text{Box}}^{\mu e e e}) G_\gamma^{\mu e*} \right] - 48s_w^4 \text{Re} [(F_Z^{\mu e} - F_\gamma^{\mu e}) G_\gamma^{\mu e*}] \\ & \left. + 32s_w^4 |G_\gamma^{\mu e}|^2 \left[ \ln \frac{m_\mu^2}{m_e^2} - \frac{11}{4} \right] \right\}, \quad (39) \end{aligned}$$

which contains the same form factors as those entering in  $\text{CR}(\mu - e, N)$ , although in different combinations, see Ref. [41, 81]. In Fig. 13b, we can see the correlation between the process  $\mu \rightarrow eee$  and  $\text{CR}(\mu - e, A_u)$ , considering

different values of the process  $\text{CR}(\mu - e, T_i)$ . As in the previous case, the star point represents the values for the benchmark point, where, according to the plot, these values are,

$$\text{BR}(\mu \rightarrow eee) \simeq 8.35 \times 10^{-16} \quad (40)$$

$$\text{CR}(\mu - e, A_u) \simeq 2.69 \times 10^{-14} \quad (41)$$

$$\text{CR}(\mu - e, T_i) \simeq 1.3 \times 10^{-14} \quad (42)$$

In turn, the light green band represents the experimental exclusion zone, where we can see that most of the values predicted by the model are below the experimental limit, including the benchmark point. From figure 13b it can be seen that the model predicts values for the observables in the ranges:  $5.57 \times 10^{-16} \lesssim \text{BR}(\mu \rightarrow eee) \lesssim 1.84 \times 10^{-15}$ ,  $1.67 \times 10^{-14} \lesssim \text{CR}(\mu - e, A_u) \lesssim 5.91 \times 10^{-14}$  and  $7.95 \times 10^{-15} \lesssim \text{CR}(\mu - e, T_i) \lesssim 2.85 \times 10^{-14}$ .

## VII. CONCLUSIONS

We have proposed a minimal extension of the SM in which the lepton-number-violating submatrix  $\mu$  of the inverse seesaw arises at *two loops*. The model adds two real singlet scalars  $\rho, \sigma$  and two generations of neutral fermions  $\nu_R, N_R, \Omega_{L,R}$ , organized under a spontaneously broken global  $U(1)_X$  and an exact  $Z_3$ . With the charge assignments in Table I, all required Yukawa interactions (11) are allowed, while a tree-level  $N$ - $\Omega$  mixing and any tree-level (or one-loop) source of  $\mu$  are forbidden. The preserved  $Z_3$  also stabilizes the lightest  $Z_3$ -nontrivial state, providing either a scalar ( $\rho$ ) or fermionic ( $\Omega$ ) dark-matter candidate.

We derived the two-loop expression for  $\mu$  and provided an analytic master representation in Appendix A. The two-loop realization naturally explains the smallness of  $\mu$  without tiny Yukawas or superheavy mediators. The active-neutrino mass matrix then follows the standard inverse-seesaw form (18), yielding three light states and two pseudo-Dirac heavy pairs with a small intra-pair splitting  $\propto \mu$ . We showed that the observed neutrino oscillation data are successfully reproduced with a representative benchmark, predicting an effective Majorana neutrino mass parameter for neutrinoless double beta decay ( $0\nu\beta\beta$ ) to be in the range  $m_{ee} \in (2.1, 4.4)$  meV for normal ordering.

On the dark-sector side, we analyzed both scalar and fermionic DM options. For scalar DM ( $m_\rho < m_\Omega$ ), annihilation proceeds dominantly via the Higgs portal into  $W^+W^-$ ,  $ZZ$ ,  $b\bar{b}$ , with direct detection controlled by the same coupling. Current XENON1T/LZ limits already push  $\lambda_{\phi\rho} \lesssim 0.1$  across most of the  $m_\rho \sim (1-3)$  TeV range, while future multi-ton detectors (XENONnT, DARWIN) will probe most of the remaining parameter space. Fermionic DM ( $m_\Omega < m_\rho$ ) mainly annihilates through  $t$ -channel  $\rho$  exchange into sterile neutrinos and is free of a tree-level Higgs portal; one-loop matching generates an effective Higgs coupling well below present bounds for  $m_\Omega \sim (1-5)$  TeV. On the other hand, this results in a significant suppression of the scattering cross section of our fermionic DM candidate off nuclei allowing reconciliation of the stringent direct DM detection constraints with the observable relic density.

Mixings between active and exotic neutrinos leads to charged-lepton-flavor violation at testable levels. For a representative benchmark we find  $\text{BR}(\mu \rightarrow e\gamma) \simeq 1.6 \times 10^{-14}$  and correlated predictions for  $\mu \rightarrow eee$  and  $\mu$ - $e$  conversion, within reach of next-generation experiments, while staying consistent with current bounds.

In summary, the same discrete symmetry that enforces the radiative origin of  $\mu$  also stabilizes dark matter, linking neutrino masses, charged lepton flavor violation, and DM phenomenology. Three natural next steps are: (i) a 1-loop RGE study to assess vacuum stability and possible Landau poles up to a chosen UV scale; (ii) a systematic exploration of CP phases (including EDM constraints); and (iii) collider recasts targeting mono- $X$  and displaced signatures of the heavy-neutral sector. Taken together with imminent direct-detection improvements, these will decisively test the favored parameter space of this two-loop inverse-seesaw framework.

### VIII. ACKNOWLEDGMENTS

R.B.B was supported by the USM Postgraduate Department, scholarship No. 037/2025 and ANID-Chile FONDECYT 1210378. GB received support from ANID-Chile FONDECYT 1210378. The work of C.B. is supported by ANID-Chile under the grant FONDECYT Regular No. 1241855. AECH is supported by ANID-Chile FONDECYT 1210378, 1241855 and ANID – Millennium Science Initiative Program *ICN2019\_044*. SK is supported by ANID-Chile FONDECYT 1230160, and ANID – Millennium Science Initiative Program *ICN2019\_044*. C. B. thanks UTFSM for its hospitality during a visit in which part of this work was completed.

#### Appendix A: Two-loop integral for Inverse seesaw $\mu$ -entry

Here, we evaluate the two-loop integral

$$I(m_1, m_2) = \int \frac{d^4 p}{(2\pi)^4} \int \frac{d^4 q}{(2\pi)^4} \frac{1}{(p^2 - m_2^2)(p^2 - m_1^2)(q^2 - m_2^2)} \frac{1}{q^2 - m_1^2} \frac{1}{(p - q)^2 - m_2^2} \quad (\text{A1})$$

introduced in Eq. (14).

After the Wick rotation we get its Euclidean representation

$$I(m_1, m_2) = \int \frac{d^4 p}{(2\pi)^4} \int \frac{d^4 q}{(2\pi)^4} \frac{1}{(p^2 + m_2^2)(p^2 + m_1^2)(q^2 + m_2^2)} \frac{1}{q^2 + m_1^2} \frac{1}{(p + q)^2 + m_2^2} \quad (\text{A2})$$

Using the identity

$$\Delta \equiv m_2^2 - m_1^2, \quad \frac{1}{(p^2 + m_1^2)(p^2 + m_2^2)} = \frac{1}{\Delta} \left( \frac{1}{p^2 + m_1^2} - \frac{1}{p^2 + m_2^2} \right), \quad (\text{A3})$$

and the analogous relation for the  $q$ -factor, we can split the double pole factors and reduce the two-loop integral (A2) to a linear combination of single-pole "sunset" integrals [82, 83]:

$$I(m_1, m_2) = \frac{1}{\Delta^2} \left[ S(m_1, m_1, m_2) - 2 S(m_1, m_2, m_2) + S(m_2, m_2, m_2) \right], \quad (\text{A4})$$

with the master formula

$$S(a, b, c) \equiv \int \frac{d^4 p}{(2\pi)^4} \int \frac{d^4 q}{(2\pi)^4} \frac{1}{(p^2 + a^2)(q^2 + b^2)((p + q)^2 + c^2)}. \quad (\text{A5})$$

A convenient Euclidean (Schwinger-parameter) representation is (see, for instance, a book [84])

$$S(a, b, c) = \frac{1}{(16\pi^2)^2} \int_0^\infty ds dt du \frac{\exp[-a^2 s - b^2 t - c^2 u]}{st + tu + us}, \quad (\text{A6})$$

which is manifestly finite for  $a, b, c > 0$  and obeys the scaling

$$S(\lambda a, \lambda b, \lambda c) = \lambda^2 S(a, b, c). \quad (\text{A7})$$

Then, we can rewrite the integral (A4) as

$$I(m_1, m_2) = \frac{1}{(16\pi^2)^2} \frac{1}{m_1^2} \mathcal{J}(x) \quad (\text{A8})$$

where  $x = m_2/m_1$  and

$$\mathcal{J}(x) = \frac{(16\pi^2)^2}{(1 - x^2)^2} [S(1, 1, x) - 2 S(1, x, x) + S(x, x, x)] \leq \max \mathcal{J}(x) = \mathcal{J}(1) \approx 1.56 \quad (\text{A9})$$

This function has no singularities and decays rapidly with increasing  $x$  roughly as  $x^{-4}$ . For estimation, we can use an approximation

$$\mathcal{J}(x) \approx \frac{z}{x^4} \quad (\text{A10})$$

The constant  $z = \mathcal{J}(1) \approx 1.56$  was determined via numerical triple integration in (A6).

- 
- [1] P. Minkowski, “ $\mu \rightarrow e\gamma$  at a Rate of One Out of  $10^9$  Muon Decays?,” *Phys. Lett. B* **67** (1977) 421–428.
  - [2] T. Yanagida, “Horizontal gauge symmetry and masses of neutrinos,” *Conf. Proc. C* **7902131** (1979) 95–99.
  - [3] S. L. Glashow, “The Future of Elementary Particle Physics,” *NATO Sci. Ser. B* **61** (1980) 687.
  - [4] R. N. Mohapatra and G. Senjanovic, “Neutrino Mass and Spontaneous Parity Nonconservation,” *Phys. Rev. Lett.* **44** (1980) 912.
  - [5] M. Gell-Mann, P. Ramond, and R. Slansky, “Complex Spinors and Unified Theories,” *Conf. Proc. C* **790927** (1979) 315–321, [arXiv:1306.4669 \[hep-th\]](#).
  - [6] J. Schechter and J. W. F. Valle, “Neutrino Masses in  $SU(2) \times U(1)$  Theories,” *Phys. Rev. D* **22** (1980) 2227.
  - [7] J. Schechter and J. W. F. Valle, “Neutrino Decay and Spontaneous Violation of Lepton Number,” *Phys. Rev. D* **25** (1982) 774.
  - [8] Y. Cai, J. Herrero-García, M. A. Schmidt, A. Vicente, and R. R. Volkas, “From the trees to the forest: a review of radiative neutrino mass models,” *Front. in Phys.* **5** (2017) 63, [arXiv:1706.08524 \[hep-ph\]](#).
  - [9] S. Jana, P. K. Vishnu, and S. Saad, “Minimal realizations of Dirac neutrino mass from generic one-loop and two-loop topologies at  $d = 5$ ,” *JCAP* **04** (2020) 018, [arXiv:1910.09537 \[hep-ph\]](#).
  - [10] C. Arbeláez, R. Cepedello, J. C. Helo, M. Hirsch, and S. Kovalenko, “How many 1-loop neutrino mass models are there?,” *JHEP* **08** (2022) 023, [arXiv:2205.13063 \[hep-ph\]](#).
  - [11] Z.-j. Tao, “Radiative seesaw mechanism at weak scale,” *Phys. Rev. D* **54** (1996) 5693–5697, [arXiv:hep-ph/9603309](#).
  - [12] D. Wyler and L. Wolfenstein, “Massless Neutrinos in Left-Right Symmetric Models,” *Nucl. Phys. B* **218** (1983) 205–214.
  - [13] R. N. Mohapatra and J. W. F. Valle, “Neutrino Mass and Baryon Number Nonconservation in Superstring Models,” *Phys. Rev. D* **34** (1986) 1642.
  - [14] M. C. Gonzalez-Garcia and J. W. F. Valle, “Fast Decaying Neutrinos and Observable Flavor Violation in a New Class of Majoron Models,” *Phys. Lett. B* **216** (1989) 360–366.
  - [15] E. K. Akhmedov, M. Lindner, E. Schnapka, and J. W. F. Valle, “Left-right symmetry breaking in NJL approach,” *Phys. Lett. B* **368** (1996) 270–280, [arXiv:hep-ph/9507275](#).
  - [16] E. K. Akhmedov, M. Lindner, E. Schnapka, and J. W. F. Valle, “Dynamical left-right symmetry breaking,” *Phys. Rev. D* **53** (1996) 2752–2780, [arXiv:hep-ph/9509255](#).
  - [17] M. Malinsky, J. C. Romao, and J. W. F. Valle, “Novel supersymmetric  $SO(10)$  seesaw mechanism,” *Phys. Rev. Lett.* **95** (2005) 161801, [arXiv:hep-ph/0506296](#).
  - [18] E. Ma, “Radiative inverse seesaw mechanism for nonzero neutrino mass,” *Phys. Rev. D* **80** (2009) 013013, [arXiv:0904.4450 \[hep-ph\]](#).
  - [19] M. Malinsky, T. Ohlsson, Z.-z. Xing, and H. Zhang, “Non-unitary neutrino mixing and CP violation in the minimal inverse seesaw model,” *Phys. Lett. B* **679** (2009) 242–248, [arXiv:0905.2889 \[hep-ph\]](#).
  - [20] F. Bazzocchi, “Minimal Dynamical Inverse See Saw,” *Phys. Rev. D* **83** (2011) 093009, [arXiv:1011.6299 \[hep-ph\]](#).
  - [21] S. S. C. Law and K. L. McDonald, “Inverse seesaw and dark matter in models with exotic lepton triplets,” *Phys. Lett. B* **713** (2012) 490–494, [arXiv:1204.2529 \[hep-ph\]](#).
  - [22] A. Abada and M. Lucente, “Looking for the minimal inverse seesaw realisation,” *Nucl. Phys. B* **885** (2014) 651–678, [arXiv:1401.1507 \[hep-ph\]](#).
  - [23] S. Fraser, E. Ma, and O. Popov, “Scotogenic Inverse Seesaw Model of Neutrino Mass,” *Phys. Lett. B* **737** (2014) 280–282, [arXiv:1408.4785 \[hep-ph\]](#).
  - [24] A. Ahriche, S. M. Boucenna, and S. Nasri, “Dark Radiative Inverse Seesaw Mechanism,” *Phys. Rev. D* **93** no. 7, (2016) 075036, [arXiv:1601.04336 \[hep-ph\]](#).
  - [25] A. E. Cárcamo Hernández, R. Martínez, and F. Ochoa, “Fermion masses and mixings in the 3-3-1 model with right-handed neutrinos based on the  $S_3$  flavor symmetry,” *Eur. Phys. J. C* **76** no. 11, (2016) 634, [arXiv:1309.6567](#)

[hep-ph].

- [26] A. E. Cárcamo Hernández, S. Kovalenko, J. W. F. Valle, and C. A. Vaquera-Araujo, “Predictive Pati-Salam theory of fermion masses and mixing,” *JHEP* **07** (2017) 118, [arXiv:1705.06320 \[hep-ph\]](#).
- [27] A. E. Cárcamo Hernández, S. Kovalenko, J. W. F. Valle, and C. A. Vaquera-Araujo, “Neutrino predictions from a left-right symmetric flavored extension of the standard model,” *JHEP* **02** (2019) 065, [arXiv:1811.03018 \[hep-ph\]](#).
- [28] A. E. Cárcamo Hernández, H. N. Long, and V. V. Vieu, “The first  $\Delta(27)$  flavor 3-3-1 model with low scale seesaw mechanism,” *Eur. Phys. J. C* **78** no. 10, (2018) 804, [arXiv:1803.01636 \[hep-ph\]](#).
- [29] E. Bertuzzo, S. Jana, P. A. N. Machado, and R. Zukanovich Funchal, “Neutrino Masses and Mixings Dynamically Generated by a Light Dark Sector,” *Phys. Lett. B* **791** (2019) 210–214, [arXiv:1808.02500 \[hep-ph\]](#).
- [30] S. Mandal, N. Rojas, R. Srivastava, and J. W. F. Valle, “Dark matter as the origin of neutrino mass in the inverse seesaw mechanism,” *Phys. Lett. B* **821** (2021) 136609, [arXiv:1907.07728 \[hep-ph\]](#).
- [31] A. E. Cárcamo Hernández and S. F. King, “Littlest Inverse Seesaw Model,” *Nucl. Phys. B* **953** (2020) 114950, [arXiv:1903.02565 \[hep-ph\]](#).
- [32] A. E. Cárcamo Hernández, J. Marchant González, and U. J. Saldaña-Salazar, “Viable low-scale model with universal and inverse seesaw mechanisms,” *Phys. Rev. D* **100** no. 3, (2019) 035024, [arXiv:1904.09993 \[hep-ph\]](#).
- [33] A. E. Cárcamo Hernández, Y. Hidalgo Velásquez, and N. A. Pérez-Julve, “A 3-3-1 model with low scale seesaw mechanisms,” *Eur. Phys. J. C* **79** no. 10, (2019) 828, [arXiv:1905.02323 \[hep-ph\]](#).
- [34] A. E. Cárcamo Hernández, D. T. Huong, and H. N. Long, “Minimal model for the fermion flavor structure, mass hierarchy, dark matter, leptogenesis, and the electron and muon anomalous magnetic moments,” *Phys. Rev. D* **102** no. 5, (2020) 055002, [arXiv:1910.12877 \[hep-ph\]](#).
- [35] A. E. C. Hernández and I. Schmidt, “A renormalizable left-right symmetric model with low scale seesaw mechanisms,” *Nucl. Phys. B* **976** (2022) 115696, [arXiv:2101.02718 \[hep-ph\]](#).
- [36] A. E. C. Hernández, D. T. Huong, and I. Schmidt, “Universal inverse seesaw mechanism as a source of the SM fermion mass hierarchy,” *Eur. Phys. J. C* **82** no. 1, (2022) 63, [arXiv:2109.12118 \[hep-ph\]](#).
- [37] A. E. C. Hernández, C. Espinoza, J. C. Gómez-Izquierdo, and M. Mondragón, “Fermion masses and mixings, dark matter, leptogenesis and  $g - 2$  muon anomaly in an extended 2HDM with inverse seesaw,” *Eur. Phys. J. Plus* **137** no. 11, (2022) 1224, [arXiv:2104.02730 \[hep-ph\]](#).
- [38] T. Nomura, H. Okada, and P. Sanyal, “A radiatively induced inverse seesaw model with hidden  $U(1)$  gauge symmetry,” *Eur. Phys. J. C* **82** no. 8, (2022) 697, [arXiv:2103.09494 \[hep-ph\]](#).
- [39] A. E. C. Hernández, H. N. Long, M. L. Mora-Urrutia, N. H. Thao, and V. V. Vieu, “Fermion masses and mixings and  $g - 2$  muon anomaly in a 3-3-1 model with  $D_4$  family symmetry,” *Eur. Phys. J. C* **82** no. 8, (2022) 769, [arXiv:2104.04559 \[hep-ph\]](#).
- [40] A. Abada, N. Bernal, A. E. C. Hernández, X. Marcano, and G. Piazza, “Gauged inverse seesaw from dark matter,” *Eur. Phys. J. C* **81** no. 8, (2021) 758, [arXiv:2107.02803 \[hep-ph\]](#).
- [41] A. Abada, N. Bernal, A. E. Cárcamo Hernández, S. Kovalenko, and T. B. de Melo, “Three-loop inverse scotogenic seesaw models,” *JHEP* **05** (2024) 035, [arXiv:2312.14105 \[hep-ph\]](#).
- [42] C. Bonilla, A. E. Cárcamo Hernández, B. Saez Díaz, S. Kovalenko, and J. Marchant Gonzalez, “Dark matter from a radiative inverse seesaw majoron model,” *Phys. Lett. B* **847** (2023) 138282, [arXiv:2306.08453 \[hep-ph\]](#).
- [43] C. Bonilla, A. E. Cárcamo Hernández, S. Kovalenko, H. Lee, R. Pasechnik, and I. Schmidt, “Fermion mass hierarchy in an extended left-right symmetric model,” *JHEP* **12** (2023) 075, [arXiv:2305.11967 \[hep-ph\]](#).
- [44] V. H. Binh, C. Bonilla, A. E. Cárcamo Hernández, D. T. Huong, V. K. N., H. N. Long, P. N. Thu, and I. Schmidt, “Phenomenology of 3-3-1 models with a radiative inverse seesaw mechanism,” *Phys. Rev. D* **110** no. 7, (2024) 075022, [arXiv:2404.13373 \[hep-ph\]](#).
- [45] A. E. Cárcamo Hernández, D. T. Huong, H. N. Long, and D. Salinas-Arizmendi, “Fermion masses and mixings and charged lepton flavor violation in a 3-3-1 model with inverse seesaw,” *PTEP* **6** (2025) 063, [arXiv:2412.18550 \[hep-ph\]](#).
- [46] D. T. Huong, A. E. Cárcamo Hernández, H. T. Hung, T. T. Hieu, and N. A. Pérez-Julve, “Extended IDM theory with low scale seesaw mechanisms,” [arXiv:2502.19488 \[hep-ph\]](#).
- [47] A. Pilaftsis, “CP violation and baryogenesis due to heavy Majorana neutrinos,” *Phys. Rev. D* **56** (1997) 5431–5451, [arXiv:hep-ph/9707235](#).
- [48] P.-H. Gu and U. Sarkar, “Leptogenesis with Linear, Inverse or Double Seesaw,” *Phys. Lett. B* **694** (2011) 226–232, [arXiv:1007.2323 \[hep-ph\]](#).
- [49] M. J. Dolan, T. P. Dutka, and R. R. Volkas, “Dirac-Phase Thermal Leptogenesis in the extended Type-I Seesaw Model,”

- JCAP* **06** (2018) 012, [arXiv:1802.08373 \[hep-ph\]](#).
- [50] C. Dib, S. Kovalenko, I. Schmidt, and A. Smetana, “Low-scale seesaw from neutrino condensation,” *Nucl. Phys. B* **952** (2020) 114910, [arXiv:1904.06280 \[hep-ph\]](#).
- [51] S. Blanchet, T. Hambye, and F.-X. Josse-Michaux, “Reconciling leptogenesis with observable  $\mu \rightarrow e \gamma$  rates,” *JHEP* **04** (2010) 023, [arXiv:0912.3153 \[hep-ph\]](#).
- [52] S. Blanchet, P. S. B. Dev, and R. N. Mohapatra, “Leptogenesis with TeV Scale Inverse Seesaw in  $SO(10)$ ,” *Phys. Rev. D* **82** (2010) 115025, [arXiv:1010.1471 \[hep-ph\]](#).
- [53] G. BHATTACHARYYA and D. DAS, “Scalar sector of two-higgs-doublet models: A minireview,” *Pramana* **87** no. 3, (Aug., 2016) . <http://dx.doi.org/10.1007/s12043-016-1252-4>.
- [54] M. Maniatis, A. von Manteuffel, O. Nachtmann, and F. Nagel, “Stability and symmetry breaking in the general two-higgs-doublet model,” *The European Physical Journal C* **48** no. 3, (Oct., 2006) 805–823. <http://dx.doi.org/10.1140/epjc/s10052-006-0016-6>.
- [55] M. E. Catano, R. Martinez, and F. Ochoa, “Neutrino masses in a 331 model with right-handed neutrinos without doubly charged Higgs bosons via inverse and double seesaw mechanisms,” *Phys. Rev. D* **86** (2012) 073015, [arXiv:1206.1966 \[hep-ph\]](#).
- [56] P. F. de Salas, D. V. Forero, S. Gariazzo, P. Martínez-Miravé, O. Mena, C. A. Ternes, M. Tórtola, and J. W. F. Valle, “2020 global reassessment of the neutrino oscillation picture,” *JHEP* **02** (2021) 071, [arXiv:2006.11237 \[hep-ph\]](#).
- [57] I. Esteban, M. C. Gonzalez-Garcia, M. Maltoni, I. Martinez-Soler, J. P. Pinheiro, and T. Schwetz, “NuFit-6.0: updated global analysis of three-flavor neutrino oscillations,” *JHEP* **12** (2024) 216, [arXiv:2410.05380 \[hep-ph\]](#).
- [58] **KamLAND-Zen** Collaboration, S. Abe *et al.*, “Search for Majorana Neutrinos with the Complete KamLAND-Zen Dataset,” [arXiv:2406.11438 \[hep-ex\]](#).
- [59] **Planck** Collaboration, N. Aghanim *et al.*, “Planck 2018 results. VI. Cosmological parameters,” *Astron. Astrophys.* **641** (2020) A6, [arXiv:1807.06209 \[astro-ph.CO\]](#). [Erratum: *Astron. Astrophys.* 652, C4 (2021)].
- [60] **XENON** Collaboration, E. Aprile *et al.*, “Dark Matter Search Results from a One Ton-Year Exposure of XENON1T,” *Phys. Rev. Lett.* **121** no. 11, (2018) 111302, [arXiv:1805.12562 \[astro-ph.CO\]](#).
- [61] **XENON** Collaboration, E. Aprile *et al.*, “Projected WIMP sensitivity of the XENONnT dark matter experiment,” *JCAP* **11** (2020) 031, [arXiv:2007.08796 \[physics.ins-det\]](#).
- [62] **LZ** Collaboration, J. Aalbers *et al.*, “Dark Matter Search Results from 4.2 Tonne-Years of Exposure of the LUX-ZEPLIN (LZ) Experiment,” [arXiv:2410.17036 \[hep-ex\]](#).
- [63] **DARWIN** Collaboration, J. Aalbers *et al.*, “DARWIN: towards the ultimate dark matter detector,” *JCAP* **11** (2016) 017, [arXiv:1606.07001 \[astro-ph.IM\]](#).
- [64] N. Bernal, A. E. Cárcamo Hernández, I. de Medeiros Varzielas, and S. Kovalenko, “Fermion masses and mixings and dark matter constraints in a model with radiative seesaw mechanism,” *JHEP* **05** (2018) 053, [arXiv:1712.02792 \[hep-ph\]](#).
- [65] M. Farina, D. Pappadopulo, and A. Strumia, “Cdm stands for constrained dark matter singlet,” *Physics Letters B* **688** no. 4–5, (May, 2010) 329–331. <http://dx.doi.org/10.1016/j.physletb.2010.04.025>.
- [66] J. Giedt, A. W. Thomas, and R. D. Young, “Dark matter, constrained minimal supersymmetric standard model, and lattice qcd,” *Physical Review Letters* **103** no. 20, (Nov., 2009) . <http://dx.doi.org/10.1103/PhysRevLett.103.201802>.
- [67] **XENON** Collaboration, E. Aprile *et al.*, “Dark Matter Search Results from a One Tonne×Year Exposure of XENON1T,” *Phys. Rev. Lett.* **121** no. 11, (2018) 111302, [arXiv:1805.12562 \[hep-ex\]](#).
- [68] **XENON** Collaboration, E. Aprile *et al.*, “First Dark Matter Search with Nuclear Recoils from the XENONnT Experiment,” *Phys. Rev. Lett.* **131** no. 4, (2023) 041003, [arXiv:2303.14729 \[hep-ex\]](#).
- [69] **LZ** Collaboration, D. S. Akerib *et al.*, “Projected wimp sensitivity of the lux-zeplin (lz) dark matter experiment,” *Phys. Rev. D* **101** (2020) 052002, [arXiv:1802.06039](#).
- [70] **DARWIN** Collaboration, J. Aalbers *et al.*, “Darwin: towards the ultimate dark matter detector,” *JCAP* **2016** no. 11, (2016) 017, [arXiv:1606.07001](#).
- [71] M. Cirelli, A. Strumia, and J. Zupan, “Dark Matter,” [arXiv:2406.01705 \[hep-ph\]](#).
- [72] A. Goyal and M. Kumar, “Fermionic Dark Matter in a simple  $t$ -channel model,” *JCAP* **11** (2016) 001, [arXiv:1609.03364 \[hep-ph\]](#).
- [73] G. Pathak, P. Das, and M. K. Das, “Neutrino mass genesis in scoto-inverse seesaw with modular  $A_4$ ,” *Eur. Phys. J. C* **85** no. 5, (2025) 569, [arXiv:2411.13895 \[hep-ph\]](#).
- [74] J. Giedt, A. W. Thomas, and R. D. Young, “Dark matter, the CMSSM and lattice QCD,” *Phys. Rev. Lett.* **103** (2009) 201802, [arXiv:0907.4177 \[hep-ph\]](#).

- [75] P. Langacker and D. London, “Lepton Number Violation and Massless Nonorthogonal Neutrinos,” *Phys. Rev. D* **38** (1988) 907.
- [76] L. Lavoura, “General formulae for  $f(1) \rightarrow f(2) \gamma$ ,” *Eur. Phys. J. C* **29** (2003) 191–195, [arXiv:hep-ph/0302221](#).
- [77] **MEG II** Collaboration, K. Afanaciev *et al.*, “New limit on the  $\mu \rightarrow e + \gamma$  decay with the MEG II experiment,” [arXiv:2504.15711 \[hep-ex\]](#).
- [78] R. Kitano, M. Koike, and Y. Okada, “Detailed calculation of lepton flavor violating muon electron conversion rate for various nuclei,” *Phys. Rev. D* **66** (2002) 096002, [arXiv:hep-ph/0203110](#). [Erratum: *Phys.Rev.D* 76, 059902 (2007)].
- [79] A. Ilakovac and A. Pilaftsis, “Flavor violating charged lepton decays in seesaw-type models,” *Nucl. Phys. B* **437** (1995) 491, [arXiv:hep-ph/9403398](#).
- [80] R. Alonso, M. Dhen, M. B. Gavela, and T. Hambye, “Muon conversion to electron in nuclei in type-I seesaw models,” *JHEP* **01** (2013) 118, [arXiv:1209.2679 \[hep-ph\]](#).
- [81] M. Lindner, M. Platscher, and F. S. Queiroz, “A Call for New Physics : The Muon Anomalous Magnetic Moment and Lepton Flavor Violation,” *Phys. Rept.* **731** (2018) 1–82, [arXiv:1610.06587 \[hep-ph\]](#).
- [82] S. P. Martin, “Evaluation of two-loop self-energy basis integrals using differential equations,” *Physical Review D* **68** (2003) 075002, [arXiv:hep-ph/0307101](#).
- [83] S. Laporta and E. Remiddi, “Analytic treatment of the two-loop equal-mass sunrise graph,” *Nuclear Physics B* **704** (2005) 349–386, [arXiv:hep-ph/0406160](#).
- [84] V. A. Smirnov, *Evaluating Feynman Integrals*. Springer, 2006.